INTERNATIONAL JOURNAL FOR NUMERICAL METHODS IN ENGINEERING
Int. J. Numer. Meth. Engng 2012; **00**:1–27
Published online in Wiley InterScience (www.interscience.wiley.com). DOI: 10.1002/nme

Fracture mechanics analysis using the wavelet Galerkin method and eXtended finite element method

S. Tanaka[1*], H. Okada[2], S. Okazawa[1], M. Fujikubo[3]

[1] *Graduate School of Engineering, Hiroshima University, 4-1 Kagamiyama 1-chome, Higashi-Hiroshima 739-8527, Japan*
[2] *Department of mechanical Engineering, Faculty of Science and Technology, Tokyo University of Science, 2641 Yamazaki, Noda 278-8510, Japan*
[3] *Graduate School of Engineering, Osaka University, 2-1 Yamadaoka, Suita, Osaka 565-0871, Japan*

SUMMARY

This paper presents fracture mechanics analysis using the wavelet Galerkin method and extended finite element method. The wavelet Galerkin method is a new methodology to solve partial differential equations where scaling/wavelet functions are used as basis functions. In solid/structural analyses, the analysis domain is divided into equally spaced structured cells and scaling functions are periodically placed throughout the domain. To improve accuracy, wavelet functions are superposed on the scaling functions within a region having a high stress concentration, such as near a hole or notch. Thus, the method can be considered a refinement technique in fixed-grid approaches. However, since the basis functions are assumed to be continuous in applications of the wavelet Galerkin method, there are difficulties in treating displacement discontinuities across the crack surface. In the present research, we introduce enrichment functions in the wavelet Galerkin formulation to take into account the discontinuous displacements and high stress concentration around the crack tip by applying the concept of the extended finite element method. This paper presents the mathematical formulation and numerical implementation of the proposed technique. As numerical examples, stress intensity factor evaluations and crack propagation analyses for two-dimensional cracks are presented. Copyright © 2012 John Wiley & Sons, Ltd.

Received . . .

KEY WORDS: Finite Element Method; Wavelet Galerkin Method; Extended Finite Element Method; Stress Intensity Factors

1. INTRODUCTION

Fracture mechanics analysis has been widely used to evaluate the integrity, safety and reliability of damaged structures such as aircraft, ships and power plants. The finite element method (FEM) is often used as a powerful computational tool to treat such crack problems. Commercial FEM software (e.g., ABAQUS, MSC.MARC and ANSYS) can produce finite element (FE) models of two-dimensional (2D) and three-dimensional (3D) cracks and calculate stress intensity factors (SIFs) using the FE models. However, the modeling of the crack and calculation of SIFs in the FE procedures still involve complicated tasks even for a skillful engineer, because special FE modeling is required; e.g., the use of double nodes to represent crack surfaces and a very fine mesh to represent stress singularities near a crack tip.

*Correspondence to: Graduate School of Engineering, Hiroshima University, 4-1 Kagamiyama 1-chome, Higashi-Hiroshima 739-8527, Japan. E-mail: satoyuki@hiroshima-u.ac.jp

Researchers have developed numerical approaches to improve computational efficiency and decrease the number of degrees of freedom (DOFs) in fracture mechanics analysis when employing the FEM. The superposition method was introduced to provide an analytical solution for stress fields near a crack tip, and FE solutions were superposed to improve the approximation of stress singularities [1]. Quarter-point elements were developed to collapse one side of the element and shift the mid-side node in the crack tip direction for isoparametric elements. The quarter-point technique can represent the $(1/\sqrt{r})$ singularity of a crack tip stress field in an elastic body [2][3][4][5][6]. As an alternative to displacement-based FEMs, hybrid singular elements [7][8][9][10][11] and the hybrid-Trefftz method [12][13][14] have been proposed. Although almost all research work treated the simple stationary crack problem, FEM was used to solve crack problem in earlier pioneering work.

Wavelet methods have been proposed as a powerful mathematical tool for representing a signal or function, and they have been applied in the research fields of signal processing and image processing [15][16][17][18][19]. In recent years, it has been found that the wavelet Galerkin method (WGM) is an efficient tool for solving partial differential equations [20][21][22]. In solid/structural analysis using the WGM, a scaling function and wavelet function are used to represent displacements or stresses. The scaling/wavelet functions have so-called multiresolution properties. The functions can produce a hierarchical structure of solutions. Furthermore, the basis functions have compact support, and the solution can be refined in regions of high gradients such as stress concentrations near a hole or notch. There are no remeshing processes in contrast to conventional FEMs. There has been much research in which the WGM with multiscale and multiresolution properties of the basis functions has been applied, such as in research on structural analysis [23][24][25][26][27][28], the solid mechanics problem [29][30][31][33], topology optimization [34][35] and the development of wavelet finite elements [36][37]. The reproducing kernel (RK) approach using wavelet hierarchical bases has also been proposed. Liu et al. [38] developed multiple scale methods using RKs and wavelet analysis. Liu et al. [39] also formulated the moving least-square reproducing kernel (MLSRK). Fourier analysis being employed to verify the approach. In the literature, the so-called synchronized convergence phenomenon was presented. Li et al. [40] proposed a synchronized reproducing kernel (SRK). Furthermore, Li et al. [41][42] proposed aRK hierarchical partition of unity. A class of basic wavelet functions is adopted to construct the hierarchical partition. An application to strain localization in inelastic solids is presented in [43] using the hierarchical partition of unity of RKs.

The multiresolution properties of the wavelet functions enhance high-stress gradients around a crack tip. However, few papers have solved fracture mechanics problems. Because most WGM basis functions are assumed to be continuous in the Galerkin formulation, there are difficulties in treating displacement jumps across the crack surface. In recent years, the extended finite element method (X-FEM) [44][45][46] has been proposed for the efficient treatment of crack problems in the framework of FEMs. New basis functions (enrichment functions) based on the concept of ”the partition of unity (PU)” [47][48] have been introduced, and they easily represent the discontinuity of the crack surface and the high-stress concentration region near the crack tip. Furthermore, the use of the X-FEM can enhance crack propagation analysis because crack geometries can be represented by enrichment functions independently of FE meshes, and the crack propagation analysis is performed without remeshing. Lee et al. [49] and Nakasumi et al. [50] proposed a coupling technique employing both the X-FEM and mesh superposition method to effectively treat crack modeling and analyze crack propagation. In addition, Li et al. [51] solved cohesive crack propagation in brittle materials using the extended Voronoi-cell finite-element model (X-VCFEM). Employing the method, polynomial functions, branch functions and multi-resolution wavelet functions are introduced to solve cohesive crack problems. The X-VCFEM was extended by adding crack merging to the growth mechanism [52].

DOI: 10.1002/nme

Fracture mechanics analyses using the WGM and X-FEM are presented for 2D crack problems in this paper. Linear B-spline scaling/wavelet basis functions [53] are used in the WG formulation. Although the basis functions do not satisfy the so-called orthogonality condition in wavelet theory, the approach is suitable for solving boundary value problems. The basis functions have an explicit form, and integration and differentiation can be performed analytically. The basis functions have compact support. In the WG discretization of solids/structures, the analysis domain is divided into equally spaced structured cells and the scaling functions are periodically placed on the grid cells. To represent the boundary of a body, a cell crossing the boundary is divided into equally spaced sub-cells. The sub-cells that are located in the external region are not involved in the numerical integration of the stiffness matrix. The method can be used to model a complicated structure automatically. Furthermore, wavelet functions having different length scales are superposed on the scaling functions to refine the solution. The method can thus be considered a refinement of the fixed-grid (voxel-type) approach [54].

In solid/structural analysis using the WGM, researchers sometimes discuss the handling of general boundaries. The fictitious domain approach [29][34] and the use of boundary-corrected wavelet functions [30][31] are commonly used. In the former, the analysis domain is extended to its exterior, but very small stiffness is given to the exterior region. In the latter, the original scaling/wavelet functions are modified so as to fit the boundary shapes. The wavelet-based finite element approach [32] is a technique that can avoid handling problems associated with boundaries. In the authors' previous study, solid mechanics problems were solved employing the WGM with B-splines [55]. Although a fictitious domain is often adopted to treat general boundaries in WGMs, a technique to remove the fictitious domain was proposed in that work. In the present paper, enrichment functions are introduced to solve crack problems on the basis of the X-FEM. A Heaviside function is enriched linear B-spline scaling function that represents discontinuous displacements of the crack surfaces. In addition, an asymptotic solution near the crack tip is enriched with both a linear B-spline scaling function and wavelet function. Crack propagation analysis is demonstrated by relocating the enrichment functions without remeshing and rebuilding the analysis model.

The layout of this paper is as follows. Section 2 presents the WG formulation for the analysis of crack problems and crack propagation analysis using the WGM and X-FEM. Section 3 presents the SIF calculation technique and discretization employing the proposed method. Numerical examples of SIF evaluations and crack propagation analyses are presented to validate the proposed technique in Section 4. Conclusions are given in Section 5.

2. FRACTURE MECHANICS ANALYSIS USING THE WGM AND X-FEM

2.1. Multiresolution properties and B-spline wavelet bases

Scaling/wavelet functions are used as basis functions in the WGM. There is a hierarchical structure of the basis functions according to the so-called multiresolution properties in wavelet theory. In this chapter, the multiresolution properties and B-spline wavelet bases are briefly presented. For more details, see references [15][16][17][18][19].

The multiresolution properties are represented by a sequence of nested closed subspaces $\{\boldsymbol{V}_j; j \in \mathbb{Z}\}$ in the Hilbert space $L^2(\mathbb{R})$,

$$\{\mathbf{0}\} \subset \cdots \subset \boldsymbol{V}_{-1} \subset \boldsymbol{V}_0 \subset \boldsymbol{V}_1 \subset \boldsymbol{V}_2 \cdots \subset L^2(\mathbb{R}). \tag{1}$$

Scaling functions are generated for these subspaces $\boldsymbol{V}_j$. The level-j scaling function $\phi_{j,k}(x)$ can be defined as

$$\phi_{j,k}(x) = 2^{j/2}\phi(2^j x - k), \quad j,k \in \mathbb{Z} \tag{2}$$

DOI: 10.1002/nme

where j is a scale parameter and k is a translate parameter. Because the space $\boldsymbol{V}_j$ lies within the space $\boldsymbol{V}_{j+1}$, any function in $\boldsymbol{V}_j$ is representable by a sum of basis functions of $\boldsymbol{V}_{j+1}$ such that

$$\phi(x) = \sum_k p_k \phi(2x - k). \tag{3}$$

This is the so-called two-scale relations of scaling functions and the set of coefficients p_k are called the two-scale sequence. Furthermore, a complementary subspace $\boldsymbol{W}_j$ to subspace $\boldsymbol{V}_j$ is introduced, such that the subspace $\boldsymbol{V}_{j+1}$ is represented by the direct sum of $\boldsymbol{W}_j$ and $\boldsymbol{V}_j$ as:

$$\boldsymbol{V}_{j+1} = \boldsymbol{V}_j + \boldsymbol{W}_j. \tag{4}$$

Wavelet functions can be generated for $\boldsymbol{W}_j$ as well as scaling functions. The level-j wavelet function $\psi_{j,k}(x)$ can be written as

$$\psi_{j,k}(x) = 2^{j/2}\psi(2^j x - k), \quad j, k \in \mathbb{Z}. \tag{5}$$

Because $\boldsymbol{W}_j$ is contained in $\boldsymbol{V}_{j+1}$, the wavelet function can be expressed in terms of the scaling function at the next higher scale with a two-scale sequence $\{q_k\}$ as:

$$\psi(x) = \sum_k q_k \phi(2x - k). \tag{6}$$

The coefficients p_k in eq. (3) and q_k in eq. (6) are defined as a set of scaling/wavelet functions.

If a set of wavelet functions, $\psi_{j,k}(x)$ in $L^2(\mathbb{R})$, form an orthonormal set, the function $\psi_{j,k}(x)$ satisfies:

$$\langle \psi_{j,k}(x) | \psi_{j',k'}(x) \rangle = \delta_{jj'}\delta_{kk'}, \tag{7}$$

where $\langle | \rangle$ represents the inner product operator and $\delta_{jj'}$ is the Kronecker delta. If an orthogonal wavelet basis set is used, the direct sum of eq. (4) becomes an orthogonal sum,

$$\boldsymbol{V}_{j+1} = \boldsymbol{V}_j \bigoplus \boldsymbol{W}_j, \quad \boldsymbol{V}_j \perp \boldsymbol{W}_j, \tag{8}$$

where $\bigoplus$ represents the orthogonal sum. Therefore, the space $L^2(\mathbb{R})$ can be decomposed by the sum of the subspaces $\boldsymbol{W}_j$ as:

$$L^2(\mathbb{R}) = \cdots \bigoplus \boldsymbol{W}_{j-1} \bigoplus \boldsymbol{W}_j \bigoplus \boldsymbol{W}_{j+1} \cdots. \tag{9}$$

A function $f(x) \in L^2(\mathbb{R})$ is approximated by its projection $P_j f(x) (= f_j(x))$ onto the space $\boldsymbol{V}_j$ as:

$$P_j f(x) = \sum_k a_{j,k} \phi_{j,k}(x). \tag{10}$$

The $P_j f(x)$ approaches $f(x)$ as $j \to \infty$. If the scaling functions $\phi_{j,k}(x)$ are orthogonal, the coefficients $a_{j,k}$ are obtained as follows:

$$a_{j,k} = \langle \phi_{j,k}(x) | f(x) \rangle. \tag{11}$$

The difference between $f(x) \in V_{j+1}$ and $P_j f(x)$ can be decomposed over the set of $\psi_{j,k}$:

$$f(x) - P_j f(x) = \sum_k b_{j,k} \psi_{j,k}(x) \in W_j, \tag{12}$$

where $b_{j,k}$ are the coefficients of the wavelet function. If the $\psi_{j,k}(x)$ are orthogonal, the coefficients are obtained as follows:

$$b_{j,k} = \langle \psi_{j,k}(x) | f(x) \rangle. \tag{13}$$

DOI: 10.1002/nme

Equations. (10) and (12) are used repeatedly with successive (j,k) values, and we thus have a hierarchical structure of the scaling/wavelet functions:

$$f_{j+1}(x) = \sum_k a_{j_0,k}\phi_{j_0,k}(x) + \sum_{i=j_0}^{j}\sum_k b_{i,k}\psi_{i,k}(x), \tag{14}$$

where $\phi_{j_0,k}(x), a_{j_0,k}$ are scaling functions with coefficients at level j_0, and $\psi_{i,k}(x), b_{i,k}(i = j_0, \cdots, j)$ are wavelet functions with coefficients at level j_0 to level j. As another representation of eq. (14), the function $f_{j+1}(x)$ can be derived by the superposition of level-$j+1$ scaling functions $\phi_{j+1,k}(x)$ with coefficients $a_{j+1,k}$ and using eq. (10), as:

$$f_{j+1}(x) = \sum_k a_{j+1,k}\phi_{j+1,k}(x). \tag{15}$$

This is the so-called multiresolution property of the scaling/wavelet functions in wavelet theory. The theory can be expanded to 2D and 3D problems in a straightforward manner. The tensor product of the 1D scaling/wavelet functions is one of the existing techniques for constructing 2D and 3D scaling/wavelet functions. The 2D representation is discussed in next section.

So far, several pairs of scaling/wavelet functions have been proposed [15][16][17][19]. B-spline wavelet bases are adopted in this research. Because the B-spline wavelet bases are bi-orthogonal wavelet family, the bases do not satisfy the orthogonality condition. The detail descriptions of the B-spline bases are written in [15][53]. On the other hand, it is possible to solve solid/structural problems in the WG formulation because the basis function has a simple form and compact support and is easy to differentiate and integrate. The m-th-order B-spline scaling/wavelet bases are represented by piecewise $(m-1)$-th-order polynomial functions, and their derivatives up to $(m-2)$-th-order are continuous. The 1D m-th-order B-spline scaling function can be written as a power series:

$$\phi^{(m)}(x) = \frac{1}{(m-1)!}\sum_{k=0}^{m}(-1)^k\ {}_mC_k(x-k)_+^{m-1} \tag{16}$$

$$x_+ = max\{0, x\} \tag{17}$$

$$x_+^m = (x_+)^m, \tag{18}$$

where the function support is

$$supp\ \phi^{(m)} = [0, m]. \tag{19}$$

The two-scale sequence $p_k(k = 0, \cdots, m)$ of the B-spline scaling function $\phi^{(m)}(x)$ in eq. (3) is

$$p_k = \frac{1}{2^{m-1}}\ {}_mC_k \tag{20}$$

In a similar way, the B-spline wavelet $\psi^{(m)}(x)$ has a two-scale sequence $q_k(k = 0, \cdots, 3m-2)$ in eq. (6):

$$q_k = \frac{(-1)^k}{2^{m-1}}\sum_l^m\ {}_mC_l\phi^{(2m)}(k+1-l). \tag{21}$$

The function support is

$$supp\ \psi^{(m)} = [0, 2m-1]. \tag{22}$$

In this analysis, linear (m=2) B-spline scaling/wavelet functions are used as wavelet Galerkin basis functions. The function forms are shown in Figs. 1 (a) and (b).

DOI: 10.1002/nme

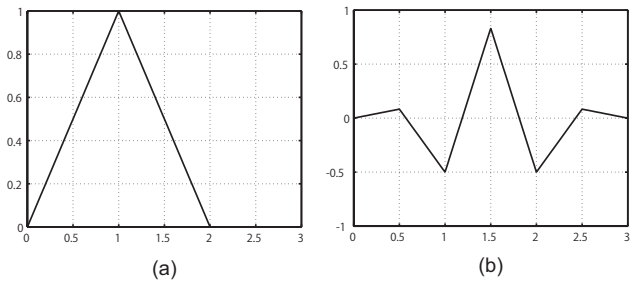

Figure 1. 1D linear (second-order) B-spline bases [(a) Scaling function, (b) Wavelet function]

2.2. Standard displacement description in a 2D WGM

Before introducing displacement fields for a crack problem in the WGM, displacement representation without a crack is first shown. The level-$j+1$ 2D displacement vector $\boldsymbol{u}_{j+1}(\boldsymbol{x})$ can be written with the level-j linear (second-order) B-spline scaling/wavelet functions as:

$$\boldsymbol{u}_{j+1}(\boldsymbol{x}) = \sum_{k,l} \boldsymbol{u}_{j,k,l} \Phi_{j,k,l}(\boldsymbol{x}) + \sum_{i=1}^{3} \sum_{k,l} \boldsymbol{v}^i_{j,k,l} \Psi^i_{j,k,l}(\boldsymbol{x}), \tag{23}$$

where $\Phi_{j,k,l}(\boldsymbol{x})$ and $\Psi^i_{j,k,l}(\boldsymbol{x})$ are level-j scaling/wavelet functions, and $\boldsymbol{u}_{j,k,l}$ and $\boldsymbol{v}^i_{j,k,l}$ $(i = 1, 2, 3)$ are their coefficients. Subscripts k and l (=$integers$) are the translation parameters. The wavelet functions can be set locally on the scaling functions where high-gradients representation is needed. The 2D scaling/wavelet functions are described by the tensor product of 1D scaling/wavelet functions as

$$\begin{aligned}
\Phi_{j,k,l}(\boldsymbol{x}) &= \phi^{(2)}_{j,k}(x_1)\phi^{(2)}_{j,l}(x_2) \\
\Psi^1_{j,k,l}(\boldsymbol{x}) &= \phi^{(2)}_{j,k}(x_1)\psi^{(2)}_{j,l}(x_2) \\
\Psi^2_{j,k,l}(\boldsymbol{x}) &= \psi^{(2)}_{j,k}(x_1)\phi^{(2)}_{j,l}(x_2) \\
\Psi^3_{j,k,l}(\boldsymbol{x}) &= \psi^{(2)}_{j,k}(x_1)\psi^{(2)}_{j,l}(x_2),
\end{aligned} \tag{24}$$

where $\phi^{(2)}_{j,k}(x_1)$ and $\phi^{(2)}_{j,l}(x_2)$ are 1D linear B-spline scaling functions and $\psi^{(2)}_{j,k}(x_1)$ and $\psi^{(2)}_{j,l}(x_2)$ are the wavelet functions for the x_1 and x_2 directions respectively. The 2D linear B-spline scaling/wavelet basis functions are shown in Figs. 2 (a)-(d). The integration domains of the 2D level-j scaling/wavelet functions are shown in Figs. 3(a)-(d). To refine the solution, 2D wavelet functions of levels $j+1, j+2, \cdots$ can be added in eq. (23). In the 2D representation, the wavelet coefficients are organized in three quadrants corresponding to the tensor products $\phi^{(2)}_{j,k}(x_1)\psi^{(2)}_{j,l}(x_2)$, $\psi^{(2)}_{j,k}(x_1)\phi^{(2)}_{j,l}(x_2)$, and $\psi^{(2)}_{j,k}(x_1)\psi^{(2)}_{j,l}(x_2)$ in the level-$j+1$ displacement vector of eq. (23). We have obtained a one-to-one decomposition of the displacements into the sum of its lower resolution approximation plus the residual associated with the wavelet coefficients. This decomposition can be iterated on the lower resolution approximation of the displacement to yield a multi-level wavelet decomposition.

Function location with different resolution levels of the linear B-spline scaling/wavelet functions are shown in Fig. 4 (a), and the 1D arrangements along x_1 direction are shown in Fig. 4 (b). The symbols represent the centers of the scaling/wavelet functions. Analysis for a level-j scaling function is assumed as the original (lowest) resolution level, and the model is called the "level-j model". The level-j scaling functions are located at the corners of the cells. In the first refinement, level-j wavelet functions are added locally to the level-j model. The centers of the wavelet functions are located between the level-j scaling functions. We thus call the model the "level-$j+1$ model".

DOI: 10.1002/nme

In a similar manner, level-$j+2$, level-$j+3\cdots$ wavelet functions are added in the second and third $\cdots$ refinements where high spatial resolution is needed. The analysis models are called the "level-$j+2$ model", "level-$j+3$ model" $\cdots$, respectively. It is thus considered that WGM is an effective refinement technique for the fixed-grid (voxel-type) approach [54].

In fracture mechanics analysis using the WGM, two approaches are adopted to accurately integrate the stiffness matrix. One is the cell refinement approach and the other is sub-cell refinement approach. The wavelet function is piecewise-linear and the function support is halved when the resolution $j \to j+1$, as shown in Fig. 4 (b). In the cell refinement approach, a structured cell is divided to accurately integrate the stiffness matrix based on the locations of the scaling/wavelet functions. Here, we define the size/resolution of the structured cells. In Fig. 4 (a), the rectangular region surrounded by the center of level-j scaling function is called the "level-j cell". A level-j cell is divided into 2×2, 4×4, and 8×8, $\cdots$ cells for the level-$j+1$, level-$j+2$, level-$j+3$, $\cdots$ models; the cells are called "level-j+1 cell", "level-j+2 cell", and "level-j+3 cell", $\cdots$. Cell refinement can be performed locally where wavelet functions are located.

In addition, a sub-cell refinement approach is adopted to accurately integrate the stiffness matrix including enrichment functions and to represent the boundary shapes. Further division is performed to the "level-j cell", "level-$j+1$ cell", and "level-$j+2$ cell", $\cdots$. For example, an illustration of a 4×4 sub-cells division is shown in Fig. 4 (c). The sub-cell refinement approach can also be adopted where the refinements are needed. In both refinement approaches, 2×2 Gauss quadrature is adopted based on the cells and sub-cells.

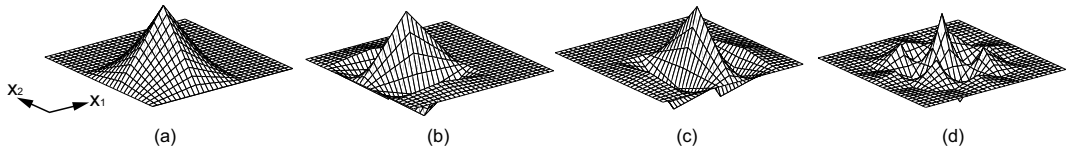

Figure 2. 2D basis functions [(a) $\Phi_{j,k,l}(\boldsymbol{x})$, (b) $\Psi^1_{j,k,l}(\boldsymbol{x})$, (c) $\Psi^2_{j,k,l}(\boldsymbol{x})$, (d) $\Psi^3_{j,k,l}(\boldsymbol{x})$]

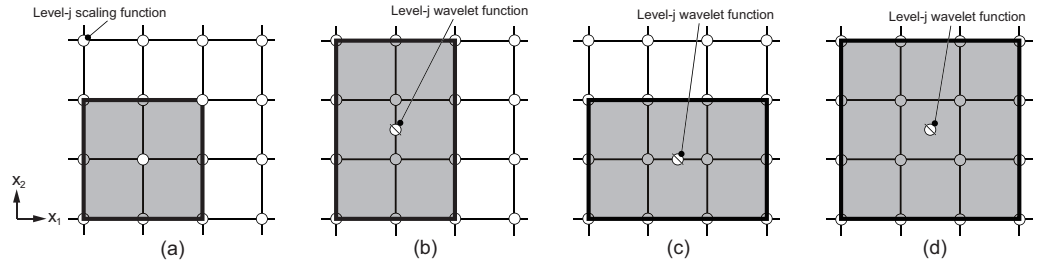

Figure 3. Integration domains for level-j scaling/wavelet functions [(a) $\Phi_{j,k,l}(\boldsymbol{x})$, (b) $\Psi^1_{j,k,l}(\boldsymbol{x})$, (c) $\Psi^2_{j,k,l}(\boldsymbol{x})$, (d) $\Psi^3_{j,k,l}(\boldsymbol{x})$]

2.3. Fracture mechanics analysis using the WGM and X-FEM

In fracture mechanics analysis using the WGM, displacements or stresses are represented by the superposition of scaling/wavelet functions as shown in eq. (23). The wavelet functions with different length scales can be superposed locally on the scaling functions. High stress gradients near a crack tip can be represented effectively by superposing the wavelet functions. However, the displacements or stresses are assumed continuous in the WG discretization, and it is difficult to treat the displacement discontinuities of crack surfaces. In this study, enrichment functions are introduced

DOI: 10.1002/nme

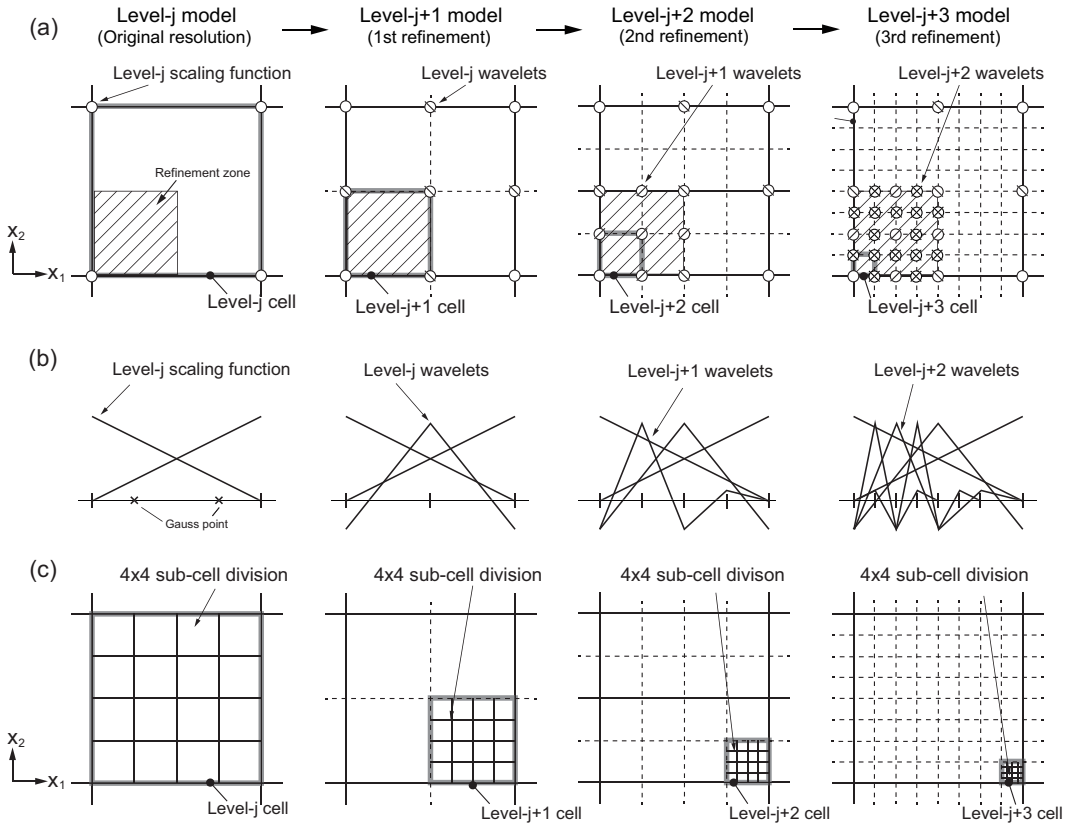

Figure 4. Refinements using wavelet functions [(a) Location of scaling/wavelet functions in 2D case and cells, (b) Location of scaling/wavelet functions in the 1D case, (c) A sub-cell refinement approach]

employing the concept of the X-FEM.

The X-FEM was proposed by [44][45] to solve crack problems. A standard FE approximation is enriched near a crack by incorporating both discontinuous fields and near-tip asymptotic fields employing the partition-of-unity (PU) method [47][48]. The method can model crack geometry independently of the FE mesh. Furthermore, crack propagation analysis can be performed easily by only relocating the enrichment functions appropriately. There are no remeshing processes. In the WG discretization, two kinds of enrichment functions are introduced as well as the X-FEM.

WG discretization for a crack problem is now described. A schematic illustration of a crack emanating from a hole edge in an elastic solid body is shown in Fig. 5(a). The analysis domain and boundary are respectively denoted Ω and Γ. The traction condition $\bar{\boldsymbol{t}}$ is enforced on Γ_t and the displacement boundary condition $\overline{\boldsymbol{u}}$ is enforced on Γ_u. The crack surface Γ_c is assumed to be traction-free. The upper-side and lower-side domains of the crack are denoted Ω_+ and Ω_-. The WG discretization is shown in Fig. 5(b). Equally spaced structured cells are used in the discretization. To accurately integrate the stiffness matrix and to represent the boundary of the body and the hole edge, cell and sub-cell refinement approaches discussed in the previous section are adopted. A cell and sub-cell, whose center is judged to be in the external domain, is not involved in the numerical integration; hence, the boundary of the body can be accurately represented. In this section, numerical formulation with level-j scaling/wavelet functions is described.

An enlarged view of the region near the crack tip is shown in Fig. 6(a). The (r, θ) coordinate system has its origin at the crack tip. The $(r, 0)$ direction is oriented into the body and parallel to

Prepared using nmeauth.cls
DOI: 10.1002/nme

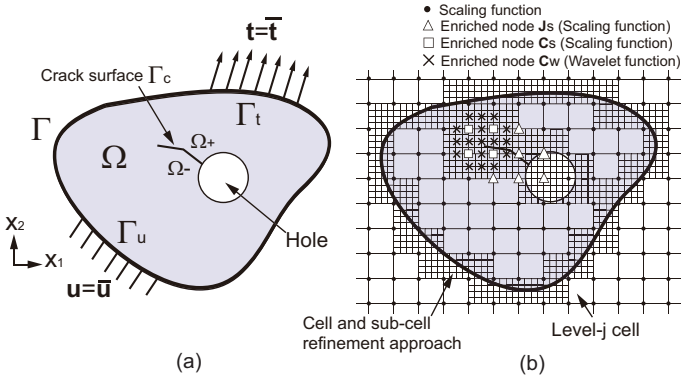

Figure 5. Crack problem for the WGM [(a) Analysis model with a crack emanating from a hole, (b) WG discretization]

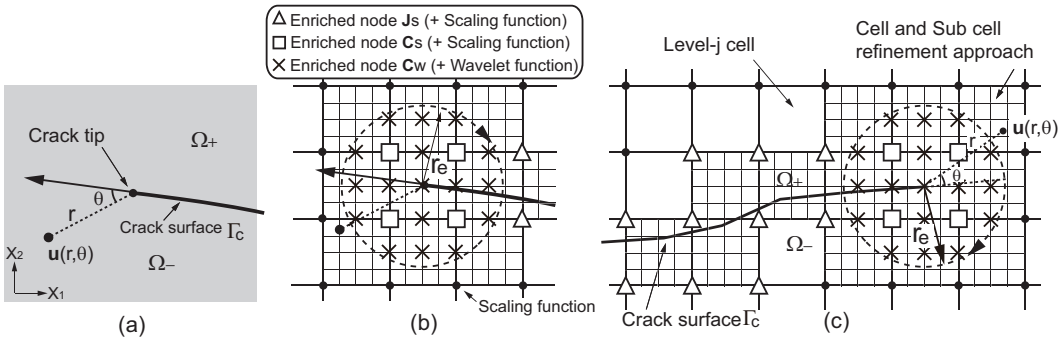

Figure 6. Enlarged view of the crack region [(a) Local coordinates (r, θ) relative to the crack tip, (b) WG modeling for a stationary crack, (c) WG modeling for crack propagation analysis]

the crack face. Crack modeling with the enrichment functions is shown in Fig. 6(b). The locations of scaling/wavelet functions and enrichment functions are presented. Here, we show an enrichment technique for a crack employing level-j scaling/wavelet functions. An enrichment function that represents the asymptotic solution near crack tip is adopted for both scaling functions and wavelet functions. Hereafter, a set of enrichment nodes is referred to as "nodes $\boldsymbol{C}_s$" for the scaling functions and "nodes $\boldsymbol{C}_w$" for the wavelet functions. The enrichment function that represents displacement jumps of the crack surface is used for scaling functions only. A set of enrichment nodes is referred to as "nodes $\boldsymbol{J}_s$". The nodes $\boldsymbol{C}_s$, $\boldsymbol{C}_w$ and $\boldsymbol{J}_s$ are presented in Fig. 6(b). In the crack modeling, level-j scaling functions are periodically set on the grids in the analysis domain. To accurately represent the severe stress concentration near the crack tip, the centers of the wavelet functions that are located within r_e of the crack tip are used. In addition, the center of the scaling/wavelet function within r_e of the crack tip is enriched as nodes $\boldsymbol{C}_s$ and $\boldsymbol{C}_w$. Although the wavelet coefficients are known to be used to predict where the refiement is needed in multiresolution analyses [27][35], radius r_e is introduced to refine the solution in this study. Furthermore, scaling functions belonging the crack surface are enriched as nodes $\boldsymbol{J}_s$ except for the nodes $\boldsymbol{C}_s$ and $\boldsymbol{C}_w$. Following the above discussion, the enriching terms are added to the level-$j+1$ displacements $\boldsymbol{u}_{j+1}(\boldsymbol{x})$ in eq. (23). The displacement $\boldsymbol{u}^{wx}_{j+1}(\boldsymbol{x})$ is written as

$$\boldsymbol{u}^{wx}_{j+1}(\boldsymbol{x}) = \sum_{k,l} \boldsymbol{u}_{j,k,l}\Phi_{j,k,l}(\boldsymbol{x}) + \sum_{i=1}^{3}\sum_{k.l} \boldsymbol{v}^i_{j,k,l}\Psi^i_{j,k,l}(\boldsymbol{x}) + \sum_{k,l\in\boldsymbol{C}_s} \Phi_{j,k,l}(\boldsymbol{x}) \sum_{n=1}^{4} \gamma_n(\boldsymbol{x})\boldsymbol{b}^n_{j,k,l}$$
$$+ \sum_{i=1}^{3}\sum_{k,l\in\boldsymbol{C}_w} \Psi^i_{j,k,l}(\boldsymbol{x}) \sum_{n=1}^{4} \gamma_n(\boldsymbol{x})\boldsymbol{c}^n_{j,k,l} + \sum_{k,l\in\boldsymbol{J}_s} H(\boldsymbol{x})\Phi_{j,k,l}(\boldsymbol{x})\boldsymbol{d}_{j,k,l}. \quad (25)$$

Prepared using nmeauth.cls
DOI: 10.1002/nme

In eq. (25), the first and second terms represent standard WG displacements as shown by eq. (23). The third and fourth terms are enrichment terms that represent the severe stress concentration around a crack tip. The third term is the enrichment with scaling functions (nodes $\boldsymbol{C}_s$), and the fourth term is the enrichment with wavelet functions (nodes $\boldsymbol{C}_w$). $\boldsymbol{b}^n_{j,k,l}$ and $\boldsymbol{c}^n_{j,k,l}$ $(n = 1, \cdots, 4)$ are the coefficients of the enrichment terms. $\gamma_n(\boldsymbol{x})$ $(n = 1, \cdots, 4)$ are functions that the asymptotic solution near the crack tip as:

$$\begin{aligned} \gamma_1(\boldsymbol{x}) = \sqrt{r}\sin\frac{\theta}{2}, \quad \gamma_2(\boldsymbol{x}) = \sqrt{r}\cos\frac{\theta}{2}, \\ \gamma_3(\boldsymbol{x}) = \sqrt{r}\sin\frac{\theta}{2}\sin\theta, \quad \gamma_4(\boldsymbol{x}) = \sqrt{r}\cos\frac{\theta}{2}\sin\theta, \end{aligned} \tag{26}$$

where (r, θ) are the local polar coordinates at the crack tip in Fig. 6(b). The fifth term represents discontinuous displacement of the crack surface enriched with level-j scaling functions. $H(\boldsymbol{x})$ is a Heaviside discontinuous function and $\boldsymbol{d}_{j,k,l}$ denotes coefficients. The scaling functions across the crack surface in the support area are enriched nodes $\boldsymbol{J}_s$ except for nodes $\boldsymbol{C}_s$ and $\boldsymbol{C}_w$. The discontinuous function $H(\boldsymbol{x})$ is

$$H(\boldsymbol{x}) = \begin{cases} 1, & (\boldsymbol{x} \in \Omega_+) \\ -1, & (\boldsymbol{x} \in \Omega_-) \end{cases}, \tag{27}$$

where Ω_+ and Ω_- are the upper and lower sides of the crack. The integration domains of the enrichment nodes $\boldsymbol{C}_s, \boldsymbol{C}_w$ and $\boldsymbol{J}_s$ with the scaling/wavelet functions are the same as those of the original scaling/wavelet functions, as shown in Fig. 3(a)-(d). The enrichment terms have discontinuity and trigonometric functions. The sub-cell refinement approach is adopted to accurately integrate the stiffness matrix including the enrichment functions and the representation of the boundaries. However, fine sub-cell refinement provides low computational efficiency; the relation between the number of sub-cell divisions and the accuracy of the solution is discussed in the numerical examples.

The PU property of this approach is briefly described. The enrichment of the discontinuous function $H(\boldsymbol{x})$ in eq. (25) is the same as that of the standard X-FEM formulation. Next, we discuss the enrichment of the asymptotic solution near the crack tip (tip enrichments) when scaling/wavelet functions are used. Eq. (25) is rearranged in terms of nodes $\boldsymbol{C}_s$ and $\boldsymbol{C}_w$ to obtain the following relation:

$$\begin{aligned} \boldsymbol{u}^{wx}_{j+1}(\boldsymbol{x}) &= \sum_{k,l} \Phi_{j,k,l}(\boldsymbol{x}) \left\{ \boldsymbol{u}_{j,k,l} + \sum_{k,l \in \boldsymbol{C}_s} \sum_{n=1}^{4} \gamma_n(\boldsymbol{x}) \boldsymbol{b}^n_{j,k,l} \right\} \\ &+ \sum_{i=1}^{3} \sum_{k,l} \Psi^i_{j,k,l}(\boldsymbol{x}) \left\{ \boldsymbol{v}^i_{j,k,l} + \sum_{k,l \in \boldsymbol{C}_w} \sum_{n=1}^{4} \gamma_n(\boldsymbol{x}) \boldsymbol{c}^n_{j,k,l} \right\}, \end{aligned} \tag{28}$$

where the first and second terms are enrichments for the scaling function and wavelet functions, respectively. We check the PU property of the scaling/wavelet functions:

$$\sum_{k,l \in \Omega} \Phi_{j,k,l}(\boldsymbol{x}) = 1, \qquad \sum_{k,l \in \Omega} \Psi^i_{j,k,l}(\boldsymbol{x}) \neq 1 \quad (i = 1, \cdots, 3). \tag{29}$$

Linear B-spline scaling functions have the PU property, but the wavelet functions do not. The lack of PU sometimes generates a loss of accuracy, e.g., [56][57][58]. Although the proposed technique cannot perfectly satisfy the PU condition, the use of wavelet function and the multiresolution properties are attractive for solving crack problems and crack propagation analyses.

Fig. 6 (c) is a schematic illustration of WG discretization for 2D crack propagation analysis. Crack propagation analysis as well as stationary-crack analysis can be performed easily by relocating the

DOI: 10.1002/nme

enrichment functions without remeshing. Although the authors proposed an adaptive strategy using the WGM [55], the same spatial resolution is kept in the step-by-step crack propagation analysis without resetting the spatial resolution. When the crack extends, scaling/wavelet functions within r_e of the crack tip are enriched using nodes $\boldsymbol{C}_s$ and $\boldsymbol{C}_w$. Scaling functions that cross the crack segment are enriched using nodes $\boldsymbol{J}_s$. The cells relating to enrichment nodes $\boldsymbol{C}_s$, $\boldsymbol{C}_w$ and $\boldsymbol{J}_s$ are divided into cells and sub-cells to perform accurate numerical integration of the stiffness matrix. The DOFs related to the enrichment functions are included in the displacements in eq. (35) and the stiffness matrix is reconstructed as shown in eq. (41). The processes are repeated incrementally in crack propagation analysis because there are no FE modeling and remeshing procedures. It is thus easy to perform crack growth simulation employing the concept of the X-FEM.

2.4. Governing equation

The governing equation for the analysis of infinitesimal small strain linearly elastostatic crack problems using the WGM and X-FEM is presented. The equation of equilibrium is

$$\nabla \cdot \boldsymbol{\sigma} + \rho \boldsymbol{g} = 0 \quad in \quad \Omega, \tag{30}$$

$$\boldsymbol{\sigma}^T \cdot \boldsymbol{n} = 0 \qquad on \quad \Gamma_c, \tag{31}$$

$$\boldsymbol{\sigma}^T \cdot \boldsymbol{n} = \bar{\boldsymbol{t}} \qquad on \quad \Gamma_t, \tag{32}$$

$$\boldsymbol{u} = \bar{\boldsymbol{u}} \qquad on \quad \Gamma_u, \tag{33}$$

where $\boldsymbol{\sigma}$ is the Cauchy stress tensor and $\boldsymbol{n}$ is the normal of the boundary Γ. ρ is the density of the body and $\boldsymbol{g}$ is the body force. On the crack surface Γ_c, traction-free condition is assumed. The linear B-spline wavelet function does not have the so-called Kronecker delta property. Thus, a penalty formulation is introduced to enforce the displacement boundary condition in eq. (33):

$$\int_\Omega \boldsymbol{\epsilon}(\delta \boldsymbol{u}^{wx}) : \boldsymbol{D} : \boldsymbol{\epsilon}(\boldsymbol{u}^{wx}) d\Omega + \alpha \int_{\Gamma_u} \delta \boldsymbol{u}^{wx} \cdot (\boldsymbol{u}^{wx} - \bar{\boldsymbol{u}})\, d\Gamma_u = \int_{\Gamma_t} \delta \boldsymbol{u}^{wx} \cdot \bar{\boldsymbol{t}}\, d\Gamma_t + \int_\Omega \delta \boldsymbol{u}^{wx} \cdot \rho \boldsymbol{g}\, d\Omega, \tag{34}$$

where $\boldsymbol{u}^{wx}$ is the displacement vector and $\delta \boldsymbol{u}^{wx}$ is its variation. $\boldsymbol{\epsilon}(\boldsymbol{u}^{wx})$ and $\boldsymbol{\epsilon}(\delta \boldsymbol{u}^{wx})$ are the symmetric parts of the displacement gradients and their variations. $\boldsymbol{D}$ denotes the elastic constants, and α is a penalty constant having a large positive value. Although the large velue for the penalty constant worsens the condition number of the stiffness matrix, it is easy to implement in the computer program and to solve linear equations because there are no additional DOFs to the system.

Eq. (25) can be rewritten in matrix form as,

$$\boldsymbol{u}^{wx}_{j+1}(\boldsymbol{x}) = \boldsymbol{N}^{wx}_{j+1}(\boldsymbol{x})\, \boldsymbol{U}^{wx}_{j+1}, \tag{35}$$

where $\boldsymbol{N}^{wx}_{j+1}(\boldsymbol{x})$ and $\boldsymbol{U}^{wx}_{j+1}$ are matrices and vectors in terms of the scaling/wavelet functions of eq. (25). Strain components are obtained by taking derivatives of eq. (35). When the resolution level-j scaling/wavelet functions are adopted, the matrix $\boldsymbol{N}^{wx}_{j+1}(\boldsymbol{x})$ can be represented as,

$$\boldsymbol{N}^{wx}_{j+1}(\boldsymbol{x}) = \left[\boldsymbol{\Phi}_j \quad \boldsymbol{\Psi}^1_j \quad \boldsymbol{\Psi}^2_j \quad \boldsymbol{\Psi}^3_j \quad \boldsymbol{\Phi}^{\boldsymbol{C}_s}_j \quad \boldsymbol{\Psi}^{1,\boldsymbol{C}_w}_j \quad \boldsymbol{\Psi}^{2,\boldsymbol{C}_w}_j \quad \boldsymbol{\Psi}^{3,\boldsymbol{C}_w}_j \quad \boldsymbol{\Phi}^{\boldsymbol{J}_s}_j \right], \tag{36}$$

where $\boldsymbol{\Phi}_j$ and $\boldsymbol{\Psi}^i_j, (i = 1, 2, 3)$ are components represented by the original level-j scaling/wavelet functions. $\boldsymbol{\Phi}^{\boldsymbol{C}_s}_j$ and $\boldsymbol{\Psi}^{i,\boldsymbol{C}_w}_j (i = 1, 2, 3)$ are represented by tip enrichment functions of nodes $\boldsymbol{C}_s$ and $\boldsymbol{C}_w$. $\boldsymbol{\Phi}^{\boldsymbol{J}_s}_j$ is an enrichment function component of nodes $\boldsymbol{J}_s$. In addition, $\boldsymbol{\Phi}^{\boldsymbol{C}_s}_j$ and $\boldsymbol{\Psi}^{i,\boldsymbol{C}_w}_j$ can be expanded as:

$$\boldsymbol{\Phi}^{\boldsymbol{C}_s}_j = \left[\boldsymbol{\Phi}^{\gamma_1}_j \quad \boldsymbol{\Phi}^{\gamma_2}_j \quad \boldsymbol{\Phi}^{\gamma_3}_j \quad \boldsymbol{\Phi}^{\gamma_4}_j \right], \tag{37}$$

Prepared using nmeauth.cls
DOI: 10.1002/nme

$$\boldsymbol{\Psi}_j^{i,\boldsymbol{C}_w} = \begin{bmatrix} \boldsymbol{\Psi}_j^{i,\gamma_1} & \boldsymbol{\Psi}_j^{i,\gamma_2} & \boldsymbol{\Psi}_j^{i,\gamma_3} & \boldsymbol{\Psi}_j^{i,\gamma_4} \end{bmatrix}, (i = 1, 2, 3). \tag{38}$$

where $\boldsymbol{\Phi}_j^{\gamma_n}$ and $\boldsymbol{\Psi}_j^{i,\gamma_n}, (n = 1, \cdots, 4)$ are components in terms of tip enrichment functions $\gamma_n(\boldsymbol{x})$ and the original scaling/wavelet functions. In a similar manner, the coefficient vectors $\boldsymbol{U}_{j+1}^{wx}$ are written as,

$$\boldsymbol{U}_{j+1}^{wx} = \begin{pmatrix} \boldsymbol{u}_j & \boldsymbol{v}_j^1 & \boldsymbol{v}_j^2 & \boldsymbol{v}_j^3 & \boldsymbol{b}_j & \boldsymbol{c}_j^1 & \boldsymbol{c}_j^2 & \boldsymbol{c}_j^3 & \boldsymbol{d}_j \end{pmatrix}^T, \tag{39}$$

where $\boldsymbol{u}_j$ and $\boldsymbol{v}_j^i, (i = 1, 2, 3)$ are coefficients for the level-j scaling/wavelet functions. $\boldsymbol{b}_j$ and $\boldsymbol{c}_j^i$ are coefficient vectors in terms of the enrichment nodes $\boldsymbol{C}_s$ and $\boldsymbol{C}_w$. $\boldsymbol{d}_j$ is the coefficient vector for enrichment nodes $\boldsymbol{J}_s$.

The expression for the displacement vector $\boldsymbol{u}_{j+1}^{wx}(\boldsymbol{x})$ in eq. (35) is substituted into eq. (34). Rearranging the equation, we obtain linear simultaneous equations for the analysis of level-j scaling/wavelet functions

$$(\boldsymbol{K}_{j+1} + \boldsymbol{K}_{j+1}^{\alpha})\boldsymbol{U}_{j+1}^{wx} = \boldsymbol{f}_{j+1} + \boldsymbol{f}_{j+1}^{\alpha} + \boldsymbol{f}_{j+1}^{\rho \boldsymbol{g}}. \tag{40}$$

$\boldsymbol{K}_{j+1}$ is stiffness matrix, which can be expanded as:

$$\boldsymbol{K}_{j+1} = \begin{pmatrix} \boldsymbol{K}_{\boldsymbol{\Phi}_j\boldsymbol{\Phi}_j} & \boldsymbol{K}_{\boldsymbol{\Phi}_j\boldsymbol{\Psi}_j^1} & \cdots & \boldsymbol{K}_{\boldsymbol{\Phi}_j\boldsymbol{\Psi}_j^3} & \boldsymbol{K}_{\boldsymbol{\Phi}_j\boldsymbol{\Phi}_j^{\boldsymbol{C}_s}} & \boldsymbol{K}_{\boldsymbol{\Phi}_j\boldsymbol{\Psi}_j^{1,\boldsymbol{C}_w}} & \cdots & \boldsymbol{K}_{\boldsymbol{\Phi}_j\boldsymbol{\Psi}_j^{3,\boldsymbol{C}_w}} & \boldsymbol{K}_{\boldsymbol{\Phi}_j\boldsymbol{\Phi}_j^{\boldsymbol{J}_s}} \\ & \boldsymbol{K}_{\boldsymbol{\Psi}_j^1\boldsymbol{\Psi}_j^1} & \cdots & \boldsymbol{K}_{\boldsymbol{\Psi}_j^1\boldsymbol{\Psi}_j^3} & \boldsymbol{K}_{\boldsymbol{\Psi}_j^1\boldsymbol{\Phi}_j^{\boldsymbol{C}_s}} & \boldsymbol{K}_{\boldsymbol{\Psi}_j^1\boldsymbol{\Psi}_j^{1,\boldsymbol{C}_w}} & \cdots & \boldsymbol{K}_{\boldsymbol{\Psi}_j^1\boldsymbol{\Psi}_j^{3,\boldsymbol{C}_w}} & \boldsymbol{K}_{\boldsymbol{\Psi}_j^1\boldsymbol{\Phi}_j^{\boldsymbol{J}_s}} \\ & & \ddots & \cdots & \cdots & \cdots & \cdots & \cdots & \cdots \\ & & & \boldsymbol{K}_{\boldsymbol{\Psi}_j^3\boldsymbol{\Psi}_j^3} & \boldsymbol{K}_{\boldsymbol{\Psi}_j^3\boldsymbol{\Phi}_j^{\boldsymbol{C}_s}} & \boldsymbol{K}_{\boldsymbol{\Psi}_j^3\boldsymbol{\Psi}_j^{1,\boldsymbol{C}_w}} & \cdots & \boldsymbol{K}_{\boldsymbol{\Psi}_j^3\boldsymbol{\Psi}_j^{3,\boldsymbol{C}_w}} & \boldsymbol{K}_{\boldsymbol{\Psi}_j^3\boldsymbol{\Phi}_j^{\boldsymbol{J}_s}} \\ & & & & \boldsymbol{K}_{\boldsymbol{\Phi}_j^{\boldsymbol{C}_s}\boldsymbol{\Phi}_j^{\boldsymbol{C}_s}} & \boldsymbol{K}_{\boldsymbol{\Phi}_j^{\boldsymbol{C}_s}\boldsymbol{\Psi}_j^{1,\boldsymbol{C}_w}} & \cdots & \boldsymbol{K}_{\boldsymbol{\Phi}_j^{\boldsymbol{C}_s}\boldsymbol{\Psi}_j^{3,\boldsymbol{C}_w}} & \boldsymbol{K}_{\boldsymbol{\Phi}_j^{\boldsymbol{C}_s}\boldsymbol{\Phi}_j^{\boldsymbol{J}_s}} \\ & & & & & \boldsymbol{K}_{\boldsymbol{\Psi}_j^{1,\boldsymbol{C}_w}\boldsymbol{\Psi}_j^{1,\boldsymbol{C}_w}} & \cdots & \boldsymbol{K}_{\boldsymbol{\Psi}_j^{1,\boldsymbol{C}_w}\boldsymbol{\Psi}_j^{3,\boldsymbol{C}_w}} & \boldsymbol{K}_{\boldsymbol{\Psi}_j^{1,\boldsymbol{C}_w}\boldsymbol{\Phi}_j^{\boldsymbol{J}_s}} \\ & \text{Sym.} & & & & & \ddots & \cdots & \cdots \\ & & & & & & & \boldsymbol{K}_{\boldsymbol{\Psi}_j^{3,\boldsymbol{C}_w}\boldsymbol{\Psi}_j^{3,\boldsymbol{C}_w}} & \boldsymbol{K}_{\boldsymbol{\Psi}_j^{3,\boldsymbol{C}_w}\boldsymbol{\Phi}_j^{\boldsymbol{J}_s}} \\ & & & & & & & & \boldsymbol{K}_{\boldsymbol{\Phi}_j^{\boldsymbol{J}_s}\boldsymbol{\Phi}_j^{\boldsymbol{J}_s}} \end{pmatrix}. \tag{41}$$

The $\boldsymbol{f}_{j+1}$ is a force vector which is also expressed as:

$$\boldsymbol{f}_{j+1} = \int_{\Gamma_t} \boldsymbol{N}_{j+1}^{wx}(\boldsymbol{x})^T \cdot \bar{\boldsymbol{t}}\, d\Gamma_t \tag{42}$$

$$\boldsymbol{f}_{j+1} = \begin{pmatrix} \boldsymbol{f}_{\boldsymbol{\Phi}_j} & \boldsymbol{f}_{\boldsymbol{\Psi}_j^1} & \cdots & \boldsymbol{f}_{\boldsymbol{\Psi}_j^3} & \boldsymbol{f}_{\boldsymbol{\Phi}_j^{\boldsymbol{C}_s}} & \boldsymbol{f}_{\boldsymbol{\Psi}_j^{1,\boldsymbol{C}_w}} & \cdots & \boldsymbol{f}_{\boldsymbol{\Psi}_j^{3,\boldsymbol{C}_w}} & \boldsymbol{f}_{\boldsymbol{\Phi}_j^{\boldsymbol{J}_s}} \end{pmatrix}^T. \tag{43}$$

In addition, matrix $\boldsymbol{K}_{j+1}^{\alpha}$ and vector $\boldsymbol{f}_{j+1}^{\alpha}$ are related to the penalty formulations. With $\boldsymbol{f}_{j+1}^{\rho \boldsymbol{g}}$ is body force vector, these can also be represented as:

$$\boldsymbol{K}_{j+1}^{\alpha} = \alpha \int_{\Gamma_u} \boldsymbol{N}_{j+1}^{wx}(\boldsymbol{x})^T \boldsymbol{N}_{j+1}^{wx}(\boldsymbol{x})\, d\Gamma_u \tag{44}$$

$$\boldsymbol{f}_{j+1}^{\alpha} = \alpha \int_{\Gamma_u} \boldsymbol{N}_{j+1}^{wx}(\boldsymbol{x})^T \cdot \bar{\boldsymbol{u}}\, d\Gamma_u \tag{45}$$

$$\boldsymbol{f}_{j+1}^{\rho \boldsymbol{g}} = \int_{\Omega} \boldsymbol{N}_{j+1}^{wx}(\boldsymbol{x})^T \cdot \rho \boldsymbol{g}\, d\Omega \tag{46}$$

where matrix $\boldsymbol{N}_{j+1}^{wx}(\boldsymbol{x})$ is represented in eq. (35) with level j scaling/wavelet functions.

DOI: 10.1002/nme

3. CALCULATION OF SIFS AND CRACK PROPAGATION ANALYSIS

A technique to calculate SIFs in 2D mixed-mode crack problems and discretization employing the WGM and X-FEM are briefly presented. The SIFs K_I and K_{II} are computed using the domain form of the interaction integral method [60]. The adoption for the analyses of X-FEM and the detailed descriptions are described [44][45][46]. K_I and K_{II} can be evaluated by splitting the J-integral [61]. Fig. 7 (a) is a schematic illustration of the domain integral. Two contours Γ_0 and Γ_1 are defined by including a crack tip. Γ_{C+} and Γ_{C-} denote upper and lower crack surfaces. The domain form can be written to be

$$J = -\int_A (W\delta_{1i} - \sigma_{ij}\frac{\partial u_j}{\partial x'_1})\frac{q(\boldsymbol{x})}{\partial x'_i}dA. \tag{47}$$

The area A is enclosed by $\Gamma(=\Gamma_0+\Gamma_{C+}+\Gamma_1+\Gamma_{C-})$ and $W(=\sigma_{ij}\epsilon_{ij})$ is strain energy. We consider two independent equilibrium states of an elastostatic solid. State 1 $J^{(1)}(u_i^{(1)},\epsilon_{ij}^{(1)},\sigma_{ij}^{(1)})(=J)$ is an actual state and State 2 $J^{(2)}(u_i^{(2)},\epsilon_{ij}^{(2)},\sigma_{ij}^{(2)})$ is auxiliary state. The auxiliary state is determined by introducing the asymptotic solution near the crack tip in linear fracture mechanics theory. The superimposed state $J^{(1+2)}(u_i^{(1+2)},\epsilon_{ij}^{(1+2)},\sigma_{ij}^{(1+2)})$ is obtained as

$$J^{(1+2)} = J^{(1)} + J^{(2)} + I^{(1+2)}, \tag{48}$$

where $I^{(1+2)}$ is the interaction integral term for both $J^{(1)}$ and $J^{(2)}$. The interaction integral for the domain integral form is

$$I^{(1+2)} = \int_A \left[\sigma_{ij}^{(1)}\frac{\partial u_i^{(2)}}{\partial x'_1} + \sigma_{ij}^{(2)}\frac{\partial u_i^{(1)}}{\partial x'_1} - W^{(1+2)}\delta_{1j}\right]\frac{\partial q(\boldsymbol{x})}{\partial x'_j}dA. \tag{49}$$

The local coordinate x'_1 is taken to be parallel to the crack face. $W^{(1+2)}(=\sigma_{ij}^{(1)}\epsilon_{ij}^{(2)}=\sigma_{ij}^{(2)}\epsilon_{ij}^{(1)})$ is the interaction strain energy. The function q($\boldsymbol{x}$) is continuous and smooth and has the property $q(\boldsymbol{x})=1$ on Γ_1 and $q(\boldsymbol{x})=0$ on Γ_0. The interaction integral in eq. (49) can be written as

$$I^{(1+2)} = \frac{2}{E'}(K_I^{(1)}K_I^{(2)} + K_{II}^{(1)}K_{II}^{(2)}), \tag{50}$$

where $K_I^{(1)}$ and $K_{II}^{(1)}$ and $K_I^{(2)}$ and $K_{II}^{(2)}$ are the SIFs of the two states. In addition, $E'=E$ for the plane strain condition and $E'=E/(1-\nu^2)$ for the plane stress condition. E is Young's modulus and ν is Poisson's ratio. When the auxiliary state is chosen as mode I (i.e., $K_I^{(2)}=1, K_{II}^{(2)}=0$) or mode II (i.e., $K_I^{(2)}=0, K_{II}^{(2)}=1$), we obtain the mode I or mode II SIFs of the actual state as

$$K_I^{(1)} = \frac{E'}{2}I^{(1+2)}, \quad K_{II}^{(1)} = \frac{E'}{2}I^{(1+2)}. \tag{51}$$

Because the WGM is based on the fixed-grid approach, it is simple to obtain the function $q(\boldsymbol{x})$ and domain A. The WG discretization for the interaction integral is shown in Fig. 7 (b). The grid points represent the locations of the centers of the lowest-resolution-level scaling functions. Here, we define the radius r_d from the crack tip. The function $q(\boldsymbol{x})$ is defined on the grids. The function $q(\boldsymbol{x})=1$ when the coordinate of the grids within r_d, and $q(\boldsymbol{x})=0$ otherwise.

Fig. 7 (c) is a schematic illustration of crack propagation analysis. We used the maximum circumferential criterion [65] to obtain the crack angle θ'. The angle θ' is calculated using the SIFs $K_I^{(1)}$ and $K_{II}^{(1)}$ according to

$$\theta' = 2tan^{-1}\frac{1}{4}\left(\frac{K_I^{(1)}}{K_{II}^{(1)}} \pm \sqrt{\left(\frac{K_I^{(1)}}{K_{II}^{(1)}}\right)^2 + 8}\right). \tag{52}$$

Prepared using nmeauth.cls
DOI: 10.1002/nme

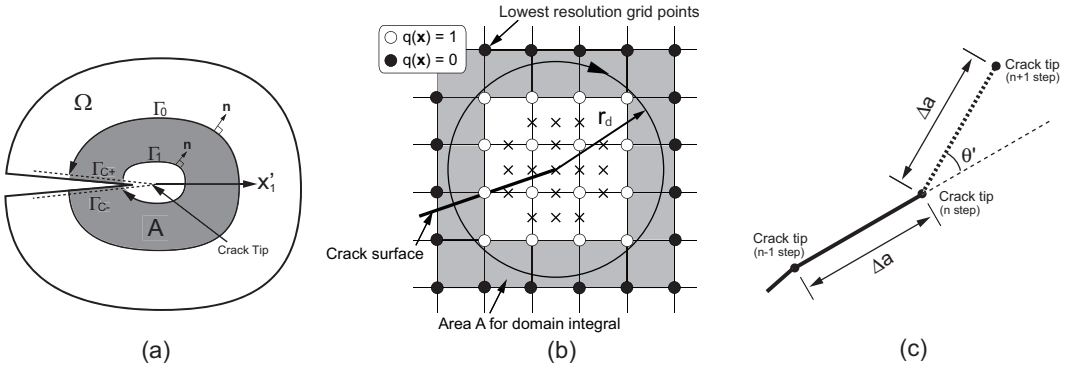

Figure 7. Calculation of SIFs [(a) Domain integral form of the J-integral, (b) Definition of the q($\boldsymbol{x}$) function in the WGM, (c) Crack extension from step n to step $n+1$]

To analyze crack propagation from step n to step $n+1$, the increment in the crack length Δa is taken to be a specified value which is small compared with the total crack length. As the crack extends, the enrichment nodes $\boldsymbol{C}_s$, $\boldsymbol{C}_w$ and $\boldsymbol{J}_s$ are relocated to fit the crack geometry. The processes are repeatedly executed in the crack propagation analysis. Fracture toughness K_{IC} will be adopted to check whether the crack has propagate or not. However, the crack path is evaluated without the use of K_{IC}.

4. NUMERICAL EXAMPLES

4.1. Rectangular plate with an edge crack

WG analysis of a rectangular plate with an edge crack is performed. The SIF K_I is evaluated to study convergence using domain integral form of J-integral of eq. (47). Fig. 8 (a) is a schematic illustration of the analysis model. The dimensions of the rectangular plate are $H = W = 10$ mm. The length of the edge crack is a = 5 mm. Uniform stress is enforced on the upper and lower edges of the plate. The WG discretization model is shown in Fig. 8 (b). In the analysis, the lowest resolution level is assumed to be as level j. The rectangular plate is divided into 15×15 equally spaced structured cells and the level-j scaling function is located on the grid points (i.e., the level-j model). To refine the solution, level-$j+1$ and level-$j+2$ models are used. The function locations of the scaling/wavelet functions are shown in Fig. 4.

4.1.1. Evaluation of the sub-cell refinement approach In the WGM, cell and sub-cell refinement approaches are adopted for the numerical integration of the stiffness matrix, as mentioned in section 2.2. The cell refinement approach is used for this integration, which includes the original scaling/wavelet functions. The sub-cell refinement approach is used for an accurate integration, which includes the enrichment functionss and to represent boundary shapes. In this section, the sub-cell refinement approach for the trigonometric function of nodes $\boldsymbol{C}_s$ and $\boldsymbol{C}_w$ are discussed.

WG crack modeling based on the X-FEM is illustrated in Fig. 8 (c). The enrichment nodes $\boldsymbol{C}_s$, $\boldsymbol{C}_w$ and $\boldsymbol{J}_s$ are used. Enrichment nodes $\boldsymbol{C}_s$ are introduced with the level-j scaling function, and $\boldsymbol{C}_w$ are introduced with level-j and level-$j+1$ wavelet functions within r_e of the crack tip. The radius r_e is set 1.0 mm. The level-$j+2$ model for r_e =1.0 mm is shown in Fig. 8 (d). J-integral is adopted to obtain SIF K_I using the domain form in eq. (47). The radius r_d for evaluating the function q($\boldsymbol{x}$) in eq. (47) is set to 5.0 mm.

DOI: 10.1002/nme

In the level-j model, a level-j cell is divided into $ndiv \times ndiv$ sub-cells. In the level-j model, a level-j+1 cell is also dividedin a similar way. The number of divisions $ndiv$ is chosen 2, 4, 8, and 16. Table I shows the calculated results of SIF K_I. When finer divisions are adopted, the SIF K_I will converge because the stiffness matrix including the enrichment functions are accurately integrated.

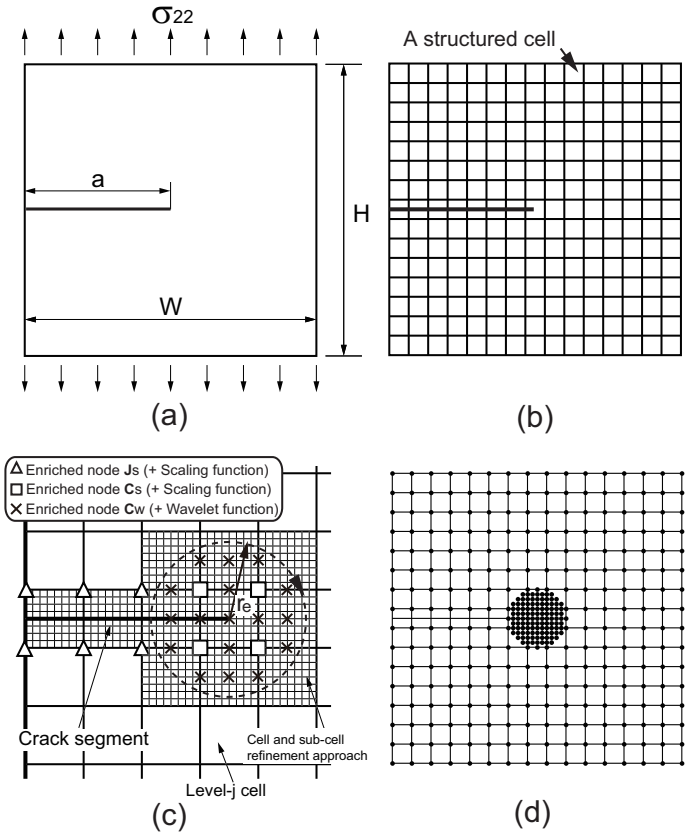

Figure 8. Rectangular plate with a edge crack [(a) Analysis model to be solved, (b) WG model (level-j model), (c) Crack modeling using nodes $\boldsymbol{C}_s$, $\boldsymbol{C}_w$, and $\boldsymbol{J}_s$, (d) WG model (level-$j+2$ model, $r_e = 1.0mm$)]

Table I. Convergence study for the sub-cell refinement approach (r_e =1.0 mm, n =4)

K_I (MPa $\sqrt{}$mm)

	Division of a sub-cell refinement approach				
ndiv x *ndiv*	1x1	2x2	4x4	8x8	16x16
Level-*j* model K_I^{Num}	13.509	11.534	11.517	11.511	11.508
Level-*j*+1 model K_I^{Num}	12.131	11.822	11.805	11.800	11.798
Level-*j*+2 model K_I^{Num}	12.010	11.841	11.832	11.829	11.828

4.1.2. Evaluation of tip enrichement functions We discuss the performance of tip enrichment functions of nodes $\boldsymbol{C}_s$ and $\boldsymbol{C}_w$. Two approaches are examined in terms of the number of enrichments $\gamma_i(\boldsymbol{x})(i = 1, \cdots, n)$ in eq. (26), i.e., n =1 and n =4. Enrichment nodes $\boldsymbol{J}_s$ are also introduced with level-j scaling functions in the crack surface area in both analyses. The radius r_e is varied among 0.6, 1.0, 1.4 and 1.8 mm. The sub-cell refinement approach ($ndiv = 4$) is adopted to accurately

Prepared using nmeauth.cls
DOI: 10.1002/nme

integrate the stiffness matrix including the enrichment functions.

The numerical results are presented in Fig. 9. In this figure, the horizontal axis gives the number of degrees of freedom and the vertical axis gives the error of K_I, which is the difference between the numerical results and the reference solution [63]. The solid lines represent the results employing one tip enrichment ($n = 1$) and the dashed lines represent the results employing four tip enrichments ($n = 4$). They represent the error in the models of level j, $j + 1$ and $j + 2$ for radii r_e=0.6, 1.0, 1.4 and 1.8 mm. The uniform-refinement models are obtained by dividing the rectangular plate into 15×15, 31×31 and 63×63 equally spaced structured cells and the analyses are performed using a scaling function only. The enrichment function $\boldsymbol{C}_s$ is set using the nodes nearest the crack tip. They can be considered as models of level j, $j + 1$ and $j + 2$ according to the standard fixed-grid (voxel-type) model employing the X-FEM. The numerical results show that the error decreases as radius r_e increases. Analyses employing four tip enrichments ($n = 4$) are more accurate than for one-tip enrichment ($n = 1$) analyses. Additionally, the solutions of models for j, $j + 1$ and $j + 2$ continuously converge although the convergence rate between the level-$j + 1$ model and level-$j + 2$ model decreases.

The path independency of the J-integral of the domain integral form is now demonstrated. The level-j, $j + 1$, and $j + 2$ model (r_e=1.0 mm) is used and the radius r_d for evaluating the function q($\boldsymbol{x}$) in eq. (47) is varied from 1.0 to 5.0 mm. Four enrichment functions (n=4) are adopted. The results are presented in Table II. The numerical results yielded better accuracy in all cases. Path independency is slightly impared when r_d =1.0 mm. In that case, the enrichment functions are included for the domain integration. Incompleteness of the PU condition seems to influence the path independency of the domain integration although the SIF is obtained with high accuracy.

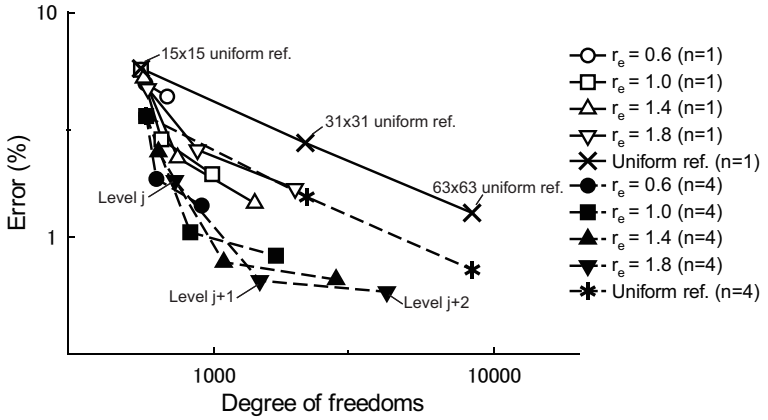

Figure 9. Convergence of K_I for the edge crack problem

Table II. Path independence of the edge crack problem (r_e =1.0 mm, n =4)

K_I (MPa $\sqrt{}$mm)

	r_d (mm)	1.0	2.0	3.0	4.0	5.0
Level-*j* model	K_I^{Num}	11.99	11.52	11.51	11.50	11.51
	Error (%)	0.51	3.47	3.49	3.59	3.53
Level-*j*+1 model	K_I^{Num}	11.85	11.81	11.80	11.79	11.80
	Error (%)	0.70	1.04	1.07	1.17	1.11
Level-*j*+2 model	K_I^{Num}	11.82	11.83	11.83	11.82	11.83
	Error (%)	0.92	0.82	0.85	0.92	0.86

DOI: 10.1002/nme

4.1.3. Examination of the accuracy for nodal density of tip enrichment functions Accuracy of the solution with different nodal densities for the tip enrichment functions is discussed. The edge crack model as shown in Fig. 8 (a) is used. The enrichment nodes $\boldsymbol{C}_s, \boldsymbol{C}_w$ and $\boldsymbol{J}_s$ are adopted. Enrichment nodes $\boldsymbol{C}_s$ are introduced with the level-j scaling function, and $\boldsymbol{C}_w$ are introduced with level-$j, j+1, \cdots, j+5$ and $j+6$ wavelet functions. Only $\gamma_1(\boldsymbol{x})(n=1)$ is adopted as the tip enrichement function for enrichments $\boldsymbol{C}_s$ and $\boldsymbol{C}_w$. Two kinds of approaches are adopted. One is with constant nodal density, i.e., r_e=0.8 mm. The other is a gradually varying nodal density, i.e., r_e =1.4 mm for level-j scaling functions and r_e=1.2, 1.0, $\cdots$, 0.4, 0.2 mm for level-$j, j+1, \cdots, j+5, j+6$ wavelet functions, respectively. The function locations at level $j+6$ model are shown in Fig. 10 (a) and (b). The convergence of the SIF K_I is presented in Fig. 11. As a comparison, the solution of the uniform refinement models (15×15, 31×31, and 63×63 equally spaced structured cell models) are also shown. Both results converge uniformly. In addition, convergence of the uniform enrichment is slow because many DOFs are needed in accordance with higher wavelet functions are adopted. In contrast, convergence is improved in the gradual enrichment approach. Although uniform enrichment is adopted in successive numerical examples, the results would imply further improvements in accuracy in fracture mechanics analysis employing WGM.

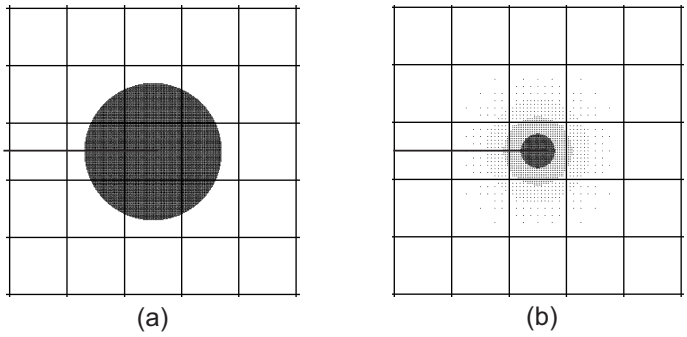

Figure 10. Location of the tip enrichment functions at level-j+6 model [(a) Nodal density is constant, (b) Nodal density is gradation]

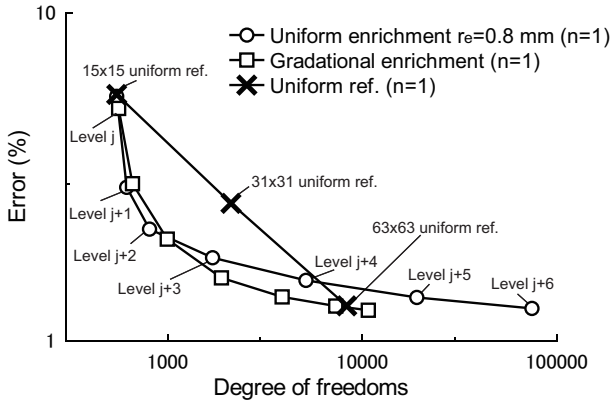

Figure 11. Convergence of K_I for the edge crack problem (n =1)

4.1.4. Condition number of different resolution WG models The condition number for different resolution models are evaluated. As the scaling/wavelet functions used are non-orgonal, higher bandwidths appear when higher resolution wavelet functions are used. Increases in condition number invite inaccuracies in the numerical solution. In addition, although direct sparse solver [68] is used in this study, convergence deterioration sometime occurs when iterative solver is adopted in the solution process. It is then important qualitative evaluation of condition numbers based on the

Prepared using nmeauth.cls
DOI: 10.1002/nme

bandwidth of the different resolution models. Edge crack model used in section 4.1.3 is examined. One tip enrichment (n =1), with radius r_e=0.8 mm and uniform nodal density, is shown in Fig. 10 (a). Eigen value analysis is performed for the stiffness matrix $\boldsymbol{K} + \boldsymbol{K}_\alpha$ in eq. (40). The penalty term $\boldsymbol{K}_\alpha$ is only used to suppress the three rigid rotation modes of the stiffness matrix. The condition number is defined as $\kappa(\boldsymbol{K} + \boldsymbol{K}_\alpha) = |\lambda_{max}/\lambda_{min}|$. λ_{max} and λ_{min} are the maximum and minimum eigen-values. The penalty constant in eq. (34) is set to α=1.0e+4. The numerical results are listed in Table. III. When higher wavelet functions are adopted, the condition number becomes larger. In section 4.1.2 and 4.1.3, the convergence studies are performed based on radius of tip enrichments and the resolution levels of the wavelet functions. In the numerical results, the convergence rate is decreased as higher wavelet functions are used in spite of the improvement of the accuracy. The results imply increase of condition number influence the impairment of the solution in the wavelet approach. In addition, because the condition number increases when large penalty constant is used, the constant should be defined appropriately.

Table III. Condition numbers for each refinement step (r_e =0.8 mm, n =1)

	level-j model	level-j+1 model	level-j+2 model	level-j+3 model	level-j+4 model	level-j+5 model
λ_{max}	6.00E+02	1.50E+03	3.08E+03	6.86E+03	1.50E+04	3.08E+04
λ_{min}	9.07E-02	9.06E-02	9.06E-02	2.68E-02	3.19E-03	3.68E-04
$\kappa(\boldsymbol{K}+\boldsymbol{K}_\alpha)$	6.62E+03	1.66E+04	3.39E+04	2.56E+05	4.70E+06	8.37E+07

Employing the proposed approach, the spatial resolution near the crack tip can be easily controlled using the wavelet functions and enrichment functions. The local refinements reduce the calculation time relative to applying the uniform-refinement model of the fixed-grid approaches. It is thus found that WG analyses using X-FEM modeling are effective in solving crack problems.

4.2. Mixed-mode problem

4.2.1. Shear edge crack problem In this section, analyses for mixed-mode problem are presented. Path independency of the interaction integral in eq. (49) is discussed first. The shear edge crack problem is chosen, as set out in Fig. 12 (a). The size of the rectangular plate and the edge crack are a/W=1/2, H/W=16/7 and W =7 mm. Shear stress τ =1.0 MPa is enforced at the top of the plate; the bottom is clamped. Level-j scaling/wavelet functions and level-j+1 wavelet function are adopted. The rectangular plate is divided into 14×32 equally spaced structured cell. Level-j scaling functions that cross the crack segment are enriched using nodes $\boldsymbol{J}_s$. The level j scaling/wavelet functions and $j+1$ wavelet function are enriched in the radius r_e =1.0 mm for nodes $\boldsymbol{C}_s$ and $\boldsymbol{C}_w$. Four tip enrichments (n=4) are specified. The sub-cell refinement approach ($ndiv$ =4) is adopted to integrate the enrichment functions $\boldsymbol{C}_s$ and $\boldsymbol{C}_w$, accurately. The WGM is shown in Fig. 12 (b). The numerical results for SIFs K_I and K_{II} are listed in Table IV (a) and (b), respectively. The error is evaluated with the reference solution of [62]. Although path independency is slightly impaired when r_d =1.0, high accuracy SIFs are obtained in all cases.

4.2.2. Rectangular plate with inclined cracks WG analyses for a rectangular plate with inclined cracks are presented. Schematic illustrations of the analysis models are presented in Fig. 13 (a)-(d). A rectangular plate with an inclined crack (model A) is solved as shown in Fig. 13 (a). The width of the rectangular plate is $2W$ =10 mm and the height is $2H$ =20 mm. The crack length is $2a$ =6 mm. The crack angle θ is varied among 15, 30, 45, 60 and 75 degrees. Uniform stress σ is enforced at the upper and lower edges of the plate. The WG model (level-$j+2$ model) for an inclined angle 45 degrees is shown in Fig. 13 (b). The rectangular plate is divided into 15×30 equally spaced structured cells and a level-j scaling function is set on the grids, and the model is assumed to be a level-j model. To refine the solution, a level-$j+2$ model is used. Level-j and level-$j+1$ wavelet functions are located within r_e=1.0 mm of each crack tip. Enrichment functions $\boldsymbol{C}_s, \boldsymbol{C}_w$ and $\boldsymbol{J}_s$ are used to model the crack. Furthermore, the problem of two cracks emanating from a hole in a

DOI: 10.1002/nme

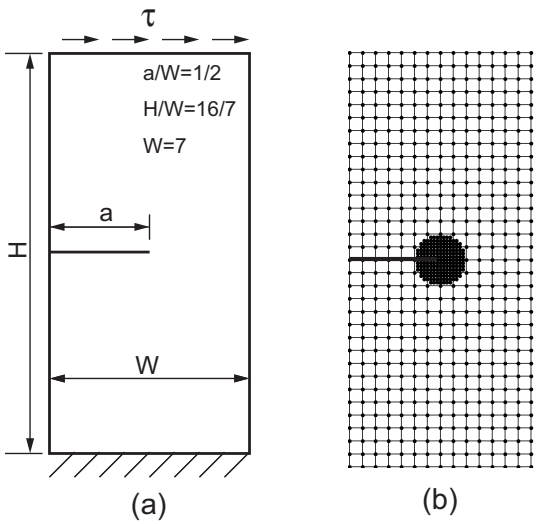

Figure 12. Shear edge crack problem [(a) rectangular plate with a edge crack, (b) WG model (level-$j+2$ model, r_e=1.0)]

Table IV. Path independency for the interaction integral for different resolution models [(a) SIF K_I, (b) SIFK_{II}]

(a)

K_I (MPa $\sqrt{}$mm)

	r_d (mm)	1.0	1.5	2.0	2.5	3.0
Level-*j* model	K_I^{Num}	33.59	33.49	33.45	33.43	33.43
	Error (%)	1.21	1.50	1.62	1.66	1.68
Level-*j*+1 model	K_I^{Num}	33.74	33.72	33.69	33.68	33.67
	Error (%)	0.75	0.83	0.92	0.95	0.96
Level-*j*+2 model	K_I^{Num}	33.75	33.74	33.71	33.70	33.70
	Error (%)	0.73	0.76	0.85	0.88	0.89

(b)

K_{II}(MPa $\sqrt{}$mm)

	r_d (mm)	1.0	1.5	2.0	2.5	3.0
Level-*j* model	K_{II}^{Num}	4.53	4.52	4.51	4.51	4.51
	Error (%)	0.35	0.58	0.79	0.81	0.79
Level-*j*+1 model	K_{II}^{Num}	4.53	4.52	4.52	4.52	4.52
	Error (%)	0.51	0.55	0.65	0.67	0.65
Level-*j*+2 model	K_{II}^{Num}	4.52	4.52	4.52	4.52	4.52
	Error (%)	0.55	0.58	0.65	0.67	0.65

rectangular plate (model B) is solved. The analysis model is shown in Fig. 13 (c). The inclined angle θ is 45 degrees. The model size and WG discretization are the same as those for model A except for the hole geometry. The hole diameter is assumed to be D=2.5 mm. The numerical integration of the stiffness matrix does not include a sub-cell whose center is judged to be within the hole. Because the WGM is based on a fixed-grid approach, it is easy to treat an arbitrary shape. The radius r_d for evaluating a function q($\boldsymbol{x}$) in eq. (49) is set to 1.5 mm for both models.

In the analyses of models A and B, the crack and hole edge intersect the cells. The sub-cell refinement approach is needed to integrate stiffness matrix including the discontinuous function of nodes $\boldsymbol{J}_s$ and to represent hole geometry. Number of division $ndiv$ for sub-cell refinement approach is discussed. Model A and model B (θ =45 degrees) in Fig. 13 (b) and (d) are chosen for the convergence studies. Four tip enrichment functions (n =4) are adopted in both cases. Analyses for

Prepared using nmeauth.cls
DOI: 10.1002/nme

model-j, $j+1$ and $j+2$ are performed. The normalized SIFs F_I and F_{II} are obtained according to F_I=$K_I/\sqrt{\pi a}$ and F_{II}=$K_{II}/\sqrt{\pi a}$. Here, F_I^{Num} and F_{II}^{Num} are the numerical results for $ndiv$ =1, 2, 4, 8, and 16. When finer divisions are adopted, the SIF K_I and K_{II} converge because the stiffness matrix including the enrichment functions and the hole edge representation is accurately integrated.

Table V. Convergence study for the sub-cell approach [(a) normalized SIF F_I, (b) normalized SIF F_{II}]

(a)

		Division of a sub-cell refinement approach				
ndiv x *ndiv*	F_I, F_{II}	1x1	2x2	4x4	8x8	16x16
Level-*j* model	F_I^{Num}	0.689	0.672	0.657	0.657	0.656
	F_{II}^{Num}	0.628	0.575	0.567	0.566	0.564
Level-*j*+1 model	F_I^{Num}	0.667	0.662	0.659	0.658	0.658
	F_{II}^{Num}	0.626	0.575	0.568	0.566	0.564
Level-*j*+2 model	F_I^{Num}	0.668	0.660	0.659	0.659	0.658
	F_{II}^{Num}	0.584	0.567	0.566	0.564	0.566

(b)

		Division of a sub-cell refinement approach				
ndiv x *ndiv*	F_I, F_{II}	1x1	2x2	4x4	8x8	16x16
Level-*j* model	F_I^{Num}	0.706	0.671	0.649	0.649	0.648
	F_{II}^{Num}	0.607	0.551	0.547	0.542	0.541
Level-*j*+1 model	F_I^{Num}	0.684	0.655	0.653	0.652	0.652
	F_{II}^{Num}	0.602	0.555	0.544	0.543	0.541
Level-*j*+2 model	F_I^{Num}	0.645	0.653	0.653	0.653	0.652
	F_{II}^{Num}	0.557	0.543	0.543	0.541	0.543

The numerical results for model A and B are shown for the inclined angle θ = 15, 30, 45, 60 and 75 degrees. Divisions for the sub-cell approach ($ndiv$ =8) is adopted. The results for model A are presented in Table VI. In addition, numerical results for model B are shown in Table VII. The results are compared with the reference solution for model A [63] and for model B [64]. In table VI and VII, F_I^{Ref}, F_{II}^{Ref} are the reference solutions. They found to be in good agreement with in both cases. The results show that the SIFs K_I and K_{II} are evaluated accurately and efficiently using the interaction integral for the domain integral form. The spatial resolution of the level-$j+2$ model near the crack tip corresponds to 60×120 uniform refinements of the fixed-grid model. The length of a structured cell (level-j cell) is l_c=1/6 mm. The ratio of the cell length (l_c) for the crack length ($2a$) is assumed to be ($l_c/2a$)=1/24. Thus, the SIFs can be calculated when the ratio $l_c/2a$ is about 1/24 when using in the proposed technique.

Table VI. Normalized SIFs F_I and F_{II} for model A

θ (deg.)	F_I^{Ref}	F_I^{Num}	F_{II}^{Ref}	F_{II}^{Num}
15	1.2183	1.2116	0.2725	0.2710
30	0.9840	0.9793	0.4800	0.4793
45	0.6611	0.6587	0.5674	0.5643
60	0.3332	0.3318	0.5022	0.5005
75	0.0896	0.0894	0.2939	0.2930

4.3. Analysis of crack propagation in a 2D rectangular plate

Crack propagation analyses for a crack in a rectangular plate are performed. The analysis model is shown in Fig. 14 (a). The dimensions of the plate are $2W = 2H$ =10 mm. The initial crack

DOI: 10.1002/nme

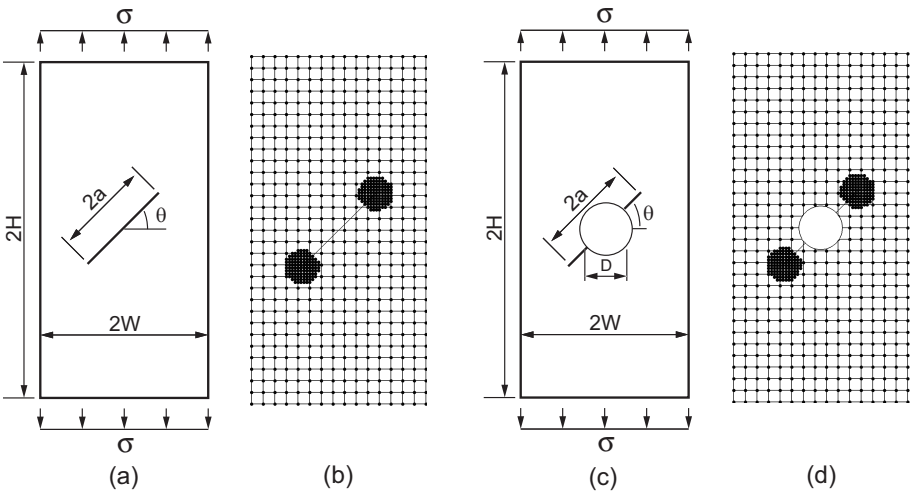

Figure 13. Rectangular plate with inclined cracks [(a) rectangular plate with a inclined crack (model A), (b) WG model for model A (level-$j+2$ model, r_e=1.0), (c) two cracks emanating from a hole in a rectangular plate (model B), (d) WG model for model B (level-$j+2$ model, r_e=1.0)]

Table VII. Normalized SIFs F_I and F_{II} for model B

θ (deg.)	F_I^{Ref}	F_I^{Num}	F_{II}^{Ref}	F_{II}^{Num}
15	1.3030	1.2913	0.2630	0.2583
30	1.0380	1.0308	0.4630	0.4616
45	0.6540	0.6528	0.5410	0.5412
60	0.2570	0.2608	0.4650	0.4669
75	-0.0290	-0.0225	0.2630	0.2648

length is assumed to be $2a$=2 mm. Young's moduls is E=3300 MPa, and Poisson's ratio is ν=0.33. Two kinds of analyses are performed. One is crack propagation analysis under uniform shear loads ($\tau_{12}=\tau_{21}$=1.0 MPa) as shown in Fig. 14 (b). The other is that under uniform tension loads (σ_{22}=1.0 MPa) as shown in Fig. 14 (c). The inclined angle of the initial crack is assumed to be θ =40 degrees. The WG model under a shear load is shown in Fig. 15 (a). The rectangular plate is divided into 63×63 equally spaced structured cells. A level-j scaling function is set on the grids. The model is assumed to be a level-j model. Level-$j+1$ models are used to refine the solution of the crack propagation analyses. Level-j wavelet functions are set on the level-j model within r_e=0.25 mm of the crack tip. The enlarged view of the shear load problem is presented in Fig. 15 (b). The increment Δa of crack propagation is assumed to be 0.35 mm in all steps. The radius r_d for the domain integral is assumed to be 0.3 mm. A sub-cell refinement approach ($ndiv$ =16) is adopted to accurately integrate the stiffness matrix including the enrichment functions $\boldsymbol{C}_s, \boldsymbol{C}_w$ and $\boldsymbol{J}_s$.

Numerical results for the shear load problem are shown in Fig. 16 (a) and those for tension problem are shown in Fig. 16 (b). The crack paths are compared with the experimental results [65]. The ratio of the cell length (l_c) to the crack length ($2a$) is assumed to be ($l_c/2a$) ≈1/25. The ratio is the same as that in Section 4.2. The crack paths are smooth and in good agreement with the reference solutions. It is thus found that crack propagation analyses using the WGM and X-FEM approach are effective.

DOI: 10.1002/nme

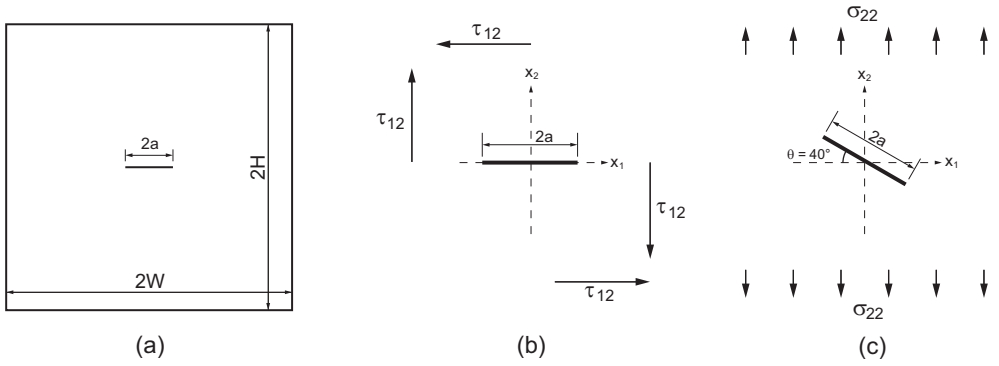

Figure 14. Crack propagation analysis for a crack in a rectangular plate [(a) A crack subjected to shear loads, (b) An inclined crack subjected to uniform tension]

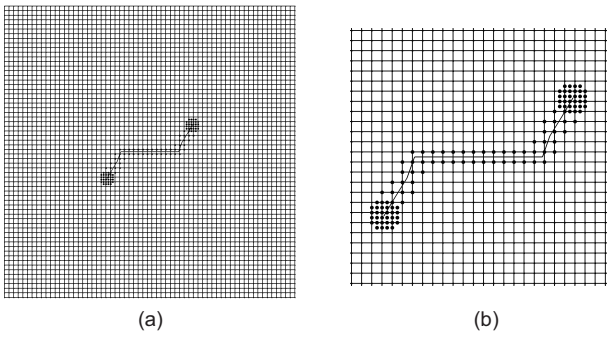

Figure 15. WG model [(a) WG model and location of enrichment functions, (b) Enlarged view]

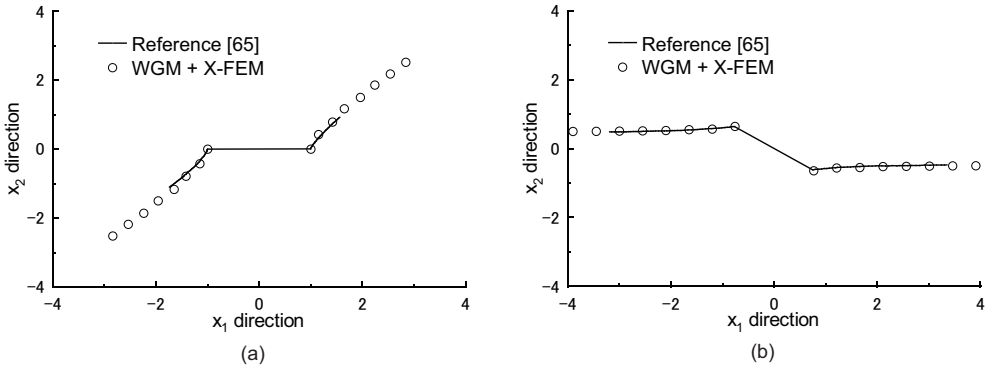

Figure 16. Numerical result with for a crack propagation in a 2D rectangular plate [(a) Shear loads problem, (b) Tension loads problem]

4.4. Crack propagation analysis for a edge crack problem

The propagation of an edge crack problem is analyzed. The experiments and numerical calculation were performed by Norikura et al. [66]. The numerical calculation is carried out employing the body force method. The analysis model is shown in Fig. 17 (a). The dimensions of the rectangular plate are $2W$=100 mm, $2H$=150 mm. The diameter of the hole is D=20 mm. Young's modulus is 3300 MPa and Poisson's ratio is ν=0.33. Uniform stress σ=1.0 MPa is enforced on the left side of the plate as the boundary condition. The initial crack size is assumed to be a=20 mm. The distance between the edge crack and the center of the hole is L=15 mm. The rectangular plate is divided into 243×162 equally spaced structured cells and the boundary hole is represented employing the

DOI: 10.1002/nme

sub-cell approach. The sub-cell refinement approach ($ndiv = 16$) is adopted. The original model is assumed to be a level-j model. Level-j scaling/wavelet functions are used as the basis functions. The level-j wavelet functions are used within r_e=1.2 mm of the crack tip. Crack propagation analyzed for Δa=1.5 and 3.0 mm. Fig. 17 (b) is a schematic illustration of the WG discretization. In addition, the radius for domain integration is assumed to be r_d=1.35 mm in all steps.

The numerical results are shown in Fig. 18. For comparison, the numerical calculation results of [66] are shown. The ratio of the cell length (l_c) to the crack length (a) is assumed to be (l_c/a) ≈1/65. The ratio is small compared with the case presented in Section 4.2. The crack paths are smooth and the analyses can be performed with high accuracy. In addition, although the crack paths are independent of the increment Δa in the initial stage, the crack tip penetrates more quickly in the small increment case (Δa=1.5 mm) when the crack tip approaches the hole edge.

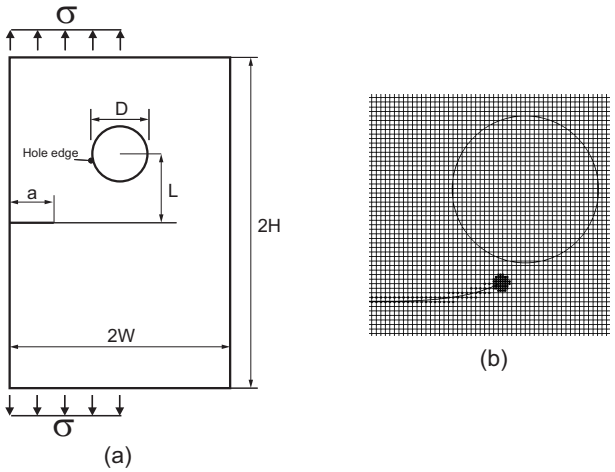

Figure 17. A edge crack propagation analysis [(a) Analysis model, (b) WG discretization model for L=15mm]

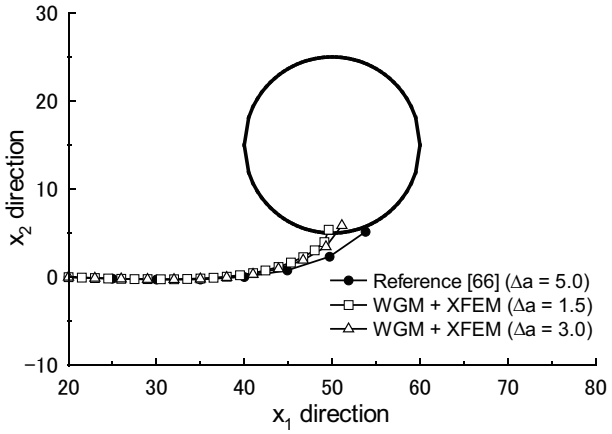

Figure 18. Numerical results for a edge crack propagation analysis

4.5. Crack propagation analysis for two parallel cracks in a rectangular plate

Crack propagation analysis for two parallel cracks in a rectangular plate is performed. The experiments and numerical simulation were performed by Higuchi et al. [67]. Schematic illustration

DOI: 10.1002/nme

of the analysis model is shown in Fig. 19 (a). The two cracks are located parallel to each other at different horizontal and vertical positions. The dimensions of the rectangular plate are $2W$=200 mm and $2H$=300 mm. Uniform stress of σ=1.0 MPa is enforced on the upper and lower edges. Young's modulus is E=210 GPa and Poisson's ratio is ν=0.3. The details of the two cracks are shown in Fig. 19 (b). The left crack is referred to as crack 1 and the right crack is referred to as crack 2. The tips of crack 1 are called tip A and tip B as shown in Fig. 19 (b). The crack length is $2a$=11 mm. The vertical distance is S=9 mm and the horizontal distance is H=15 mm. The analysis model is divided into 324×216 equally spaced structured cells. The sub-cell refinement approach ($ndiv = 16$) is adopted. The model is assumed to be a level-j model, and level-j scaling functions are set on the grid points. In the analysis, level-j scaling/wavelet functions are used. The level-j functions are used within r_e=0.7 mm of the center of the crack tips. The increment Δa in each step is assumed to be 1.1 mm. The WG crack modeling using X-FEM is shown in Fig. 19 (c). The radius for the domain integral is assumed to be r_d=0.9 mm.

Crack paths and behaviors are shown in Figs. 20 (a)-(h). The horizontal distance between two cracks is denoted as S', and the vertical distance is denoted 2a' in these figures. The crack propagation behaviors are follows. The cracks extend independently from step (a) to step (b). The cracks overlap in at step (c). The crack tips approach each other from step (d) to step (h). Finally, the cracks connect. The SIFs of tip A and tip B of crack 1 are shown in Table. VIII. The SIF K_I^B of tip B takes a maximum value in step (d). At the same time, the SIF K_{II}^B slightly increases. The behaviors of the SIFs are considered to explain the deflection of the crack tips. The crack paths are compared with the reference solution [67] and found to coincide well. The ratio of the cell length (l_c) to the crack length ($2a$) is assumed to be ($l_c/2a$) ≈1/24. It is thus considered that the analyses can be performed with high accuracy.

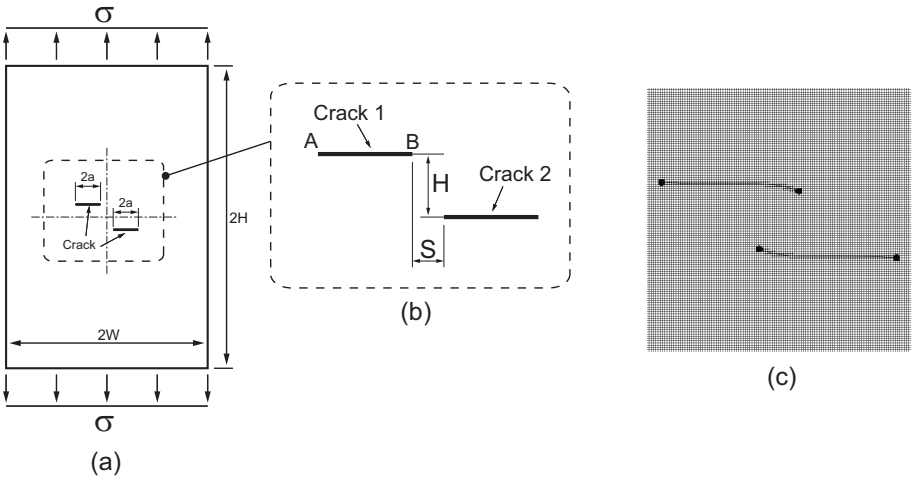

Figure 19. Crack propagation for two parallel cracks [(a) Analysis model to be solved, (b) Enlarged view of the two cracks, (c) WG model]

5. CONCLUSION

This paper presented fracture mechanics analyses using the WGM and X-FEM for 2D crack problems. Linear B-spline scaling/wavelet basis functions were used as basis functions. Enrichment functions were introduced to solve crack problems according to the concept of the X-FEM. A Heaviside function, which is an enriched linear B-spline scaling function that represents discontinuous displacements of the crack surfaces, was used. In addition, the asymptotic solution

DOI: 10.1002/nme

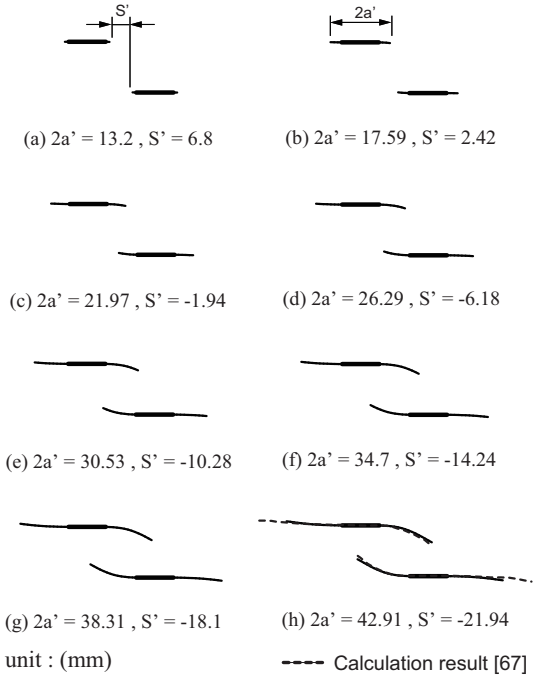

Figure 20. Crack paths of the two parallel cracks

Table VIII. SIFs for tip A and tip B (crack 1)

	K_I^A	K_{II}^A	K_I^B	K_{II}^B
(a)	4.87	0.01	4.87	-0.01
(b)	5.89	0.03	5.79	0.10
(c)	6.98	0.04	6.50	0.19
(d)	8.12	0.06	6.84	0.19
(e)	9.30	0.06	6.83	0.15
(f)	10.50	0.05	6.55	0.08
(g)	11.80	0.07	6.14	0.01
(h)	13.19	0.04	5.70	-0.03

near the crack tip was enriched by both a linear B-spline scaling function and wavelet function to represent the severe stress concentration around the crack tip. Crack propagation analysis was demonstrated by relocating the enrichment functions without remeshing and rebuilding the analysis model. Numerical examples of SIFs evaluations and crack propagation analyses were presented to validate the proposed technique. The WG approach based on the X-FEM was found to be effective for crack problems and crack propagation analysis.

5.1. Acknowledgements

A part of present research conducted by Satoyuki Tanaka was financially supported by The Research Council of Norway (RCN) through the Yggdrasil mobility programme.

REFERENCES

1. Yamamoto Y., Tokuda N., (1973), Determination of stress intensity factor in cracked plates by the finite element method, International Journal for Numerical Methods in Engineering, 6, pp. 427-439.

DOI: 10.1002/nme

2. Henshell R. D., Shaw K. G., (1975), Crack tip finite elements are unnecessary, International Journal for Numerical Methods in Engineering, 9, pp. 495-507.
3. Barsoum R. S., (1976), On the use of isoparametric finite elements in linear fracture mechanics, International Journal for Numerical Methods in Engineering, 10, pp. 25-37.
4. Barsoum R. S., (1977), Triangular quarter-point elements as elastic and perfectly-plastic crack tip elements, International Journal for Numerical Methods in Engineering, 11, pp. 85-98.
5. Hibbit H. D., (1977), Some properties of singular isoparametric elements, International Journal for Numerical Methods in Engineering, 11, pp. 180-184.
6. Banks-Sills L., Bortman Y., (1984), Reappraisal of the quarter-point quadrilateral element in linear elastic fracture mechanics, International Journal of Fracture, 25, pp. 169-180.
7. Tong P., Pian T. H. H., Lasry S. J., (1973), A hybrid-element approach to crack problems in plane elasticity, International Journal for Numerical Methods in Engineering, 7, pp. 297-308.
8. Tong P., (1977), A hybrid crack element for rectilinear anisotropic material, International Journal for Numerical Methods in Engineering, 11, pp. 377-382.
9. Lin K. Y., Tong P., (1980), Singular finite elements for the fracture analysis of v-notched plate, International Journal for Numerical Methods in Engineering, 15, pp. 1343-1354.
10. Piltner R., (1985), Special finite elements with holes and internal cracks, International Journal for Numerical methods in Engineering, 21, pp. 1471-1485.
11. Zeng D., Katsube N., Zhang J., Soboyejo W., (2002), Hybrid crack-tip element and its applications, Finite Elements in Analysis and Design, 38, pp. 319-335.
12. Jirousek S. J., (1987), Hybrid-Trefftz plate bending elements with p-method capabilities, International Journal for Numerical Methods in Engineering, 24, pp. 1367-1393.
13. Jirousek J., Venkatesh A., Zielinski A. P., Rabemanantsoa H., (1993), Comparative study of p-extensions based on conventional assumed displacement and hybrid-Trefftz fe models, Computers & Structures, 46, pp. 261-278.
14. Teixeira de Freitas J. A., Cismaşiu C., (1999), Numerical implementation of hybrid-Trefftz displacement elements, Computers & Structures, 73, pp. 207-225.
15. Chui C. K., (1992), An introduction to wavelets, Academic Press.
16. Daubechies I., (1992), Ten Lectures on Wavelets, SIAM, Philadelphia.
17. Mayer Y. (1993), Wavelets: Algorithms and Applications, SIAM, Philadelphia.
18. Williams J. R., Amaratunga K., (1994), Introduction to wavelets in engineering, International Journal for Numerical Methods in Engineering, 37, pp. 2365-2388.
19. Chui C. K., (1997), Wavelets: A Mathematical Tool for Signal Analysis, SIAM, Phiradelphia.
20. Amaratunga K., Williams J. R., (1993), Wavelet based Green's function approach to 2D PDEs, Engineering Computations, 10, pp. 349-367.
21. Amaratunga K. Williams J. R., Qian S. and John W., (1994), Wavelet-Galerkin solutions for one-dimensional partial differential equations, International Journal for Numerical Methods in Engineering, 37, pp. 2703-2716.
22. Christon M. A., Roach D. W., (2000), The numerical performance of wavelets for PDEs: the multi-scale finite element, Computational Mechanics, 25, pp. 230-244.
23. Chen W. H., Wu C. W., (1995), A spline wavelets element method for frame structures vibration, Computational Mechanics, 16, pp. 11-21.
24. Wu C. W., Chen W. H., (1996), Extension of spline wavelets element method to membrane vibration analysis, Computational Mechanics, 18, pp. 46-54.
25. Youhe Z., Jizeng W. and Xiaojing, Z., (1998), Applications of wavelet Galerkin FEM to bending of beam and plate structures, Applied Mathematics and Mechanics, 19, pp. 745-755.
26. Kim Y. Y., Jang G. W., (2002), Hat interpolation wavelet-based multi-scale Galerkin method for thin-walled box beam analysis, International Journal for Numerical Methods in Engineering, 53, pp. 1575-1592.
27. Jang G. W., Kim J. E. and Kim Y. Y., (2004), Multiscale Galerkin method using interpolations wavelets for two-dimensional elliptic problems in general domains, International Journal for Numerical Methods in Engineering, 59, pp. 225-253.
28. Han J. G., Ren W. X., Huang Y., (2006), A spline wavelet finite-element method in structural mechanics, International Journal for Numerical Methods in Engineering, 66, pp. 166-190.
29. Diaz A. R., (1999), A wavelet-Galerkin scheme for analysis of large-scale analysis on simple domains, International Journal for Numerical Methods in Engineering, 44, pp. 1599-1616.
30. Venini P. and Morana P., (2001), An adaptive wavelet-Galerkin method for an elastic-plastic-damage constitutive model: 1D problem, Computer Methods in Applied Mechanics and Engineering, 190, pp. 5619-5638.
31. Cominciol V., Scapolla T., Naldi G. and Venini P. (2000), A wavelet-like Galerkin method for numerical solution of variational inequalities arising in elastoplasticity, Communications in Numerical Methods in Engineering, 16, pp. 133-144.
32. Han J. G., Ren W. X., Huang Yih, (2006), A spline wavelet finite-element method in structural mechanics, International Journal for Numerical Methods in Engineering, 66, pp. 166-190.
33. Liu Y., Qin F., Liu Y., Cen Z., (2010), The 2D large deformation analysis using Daubechies wavelet, Computational Mechanics, 45, pp. 179-187.
34. DeRose Jr. C. G. A., Diaz A. R., (2000), Solving three-dimensional layout optimization problems using fixed scale wavelets, Computational Mechanics, 25, pp. 274-285.
35. Kim J. E., Jang G. W. and Kim Y. Y., (2003), Adaptive multiscale wavelet-Galerkin analysis for plane elasticity problems and its application to multiscale topology design optimization, International Journal of Solids and Structures., 40, pp. 6473-6496.
36. Xiang J. W., Chen X. F., He Z. J., Dong H. B., (2007), The construction of 1D wavelet finite elements for structural analysis, Computational Mechanics, 40, pp. 325-339.
37. Quraishi S. M., Sandeep K., (2011), A second generation wavelet based finite elements on triangulations, Computational Mechanics, 48, pp. 163-174.

DOI: 10.1002/nme

38. Liu W. K, Chen Y., (1995), Wavelet and multiple scale reproducing kernel methods, International Journal for Numerical Methods in Fluids, 21, pp. 901-931.
39. Li S., Liu W. K., (1996), Moving least-square reproducing kernel method Part II: Fourier analysis, Computer Methods in Applied Mechanics and Engineering, 139, pp. 159-193.
40. Li S., Liu W. K., (1998), Synchronized reproducing kernel interpolant via multiple wavelet expansion, Computational Mechanics, 21, pp. 28-47.
41. Li S., Liu W. K., (1999), Reproducing Kernel Hierarchical Partition of Unity, Part I - Formulation and Theory, International Journal for Numerical Methods in Engineering, 45, pp. 251-288.
42. Li S., Liu W. K., (1999), Reproducing Kernel Hierarchical Partition of Unity, Part II - Applications, International Journal for Numerical Methods in Engineering, 45, pp. 289-317.
43. Li S., Liu W. K., (2000), Numerical simulations of strain localization in inelastic solids using mesh-free methods, International Journal for Numerical Methods in Engineering, 48, pp. 1285-1309.
44. Belytschko T., Black T., (1999), Elastic crack growth in finite elements with minimal remeshing, International Journal for Numerical Methods in Engineering, 45, pp. 601-620.
45. Moës N., Dolbow J., Belytschko T., (1999), A finite element method for crack growth without remeshing, International Journal for Numerical Methods in Engineering, 46, pp. 131-150.
46. Dolbow J., Moës N., Belytschko T., (2000), Discontinuous enrichment in finite elements with a partition of unity method, Finite Elements in Analysis and Design, 36, pp. 235-260.
47. Melenk J. M., Babuška I., (1996), The partition of unity finite element method: basic theory and applications., Computer Methods in Applied Mechanics and Engineering, 139, pp. 289-314.
48. Babuška I., Melenk J. M., (1997), The partition of unity method, International Journal for Numerical Methods in Engineering, 40, pp. 727-758.
49. Lee S. H., Song J. H., Yoon Y. C., Zi G., Belytschko T., (2004), Combined extended and superimposed finite element method for cracks, International Journal for Numerical Methods in Engineering, 59, pp. 1119-1136.
50. Nakasumi S., Suzuki K., Ohtsubo H., (2008), Crack growth analysis using mesh superposition technique and X-FEM, International Journal for Numerical Methods in Engineering, 75, pp. 291-304.
51. Li S., Ghosh S., (2006), Extended Voronoi cell finite element model for multiple cohesive crack propagation in brittle materials, International Journal for Numerical Methods in Engineering, 65, pp. 1028-1067.
52. Li S., Ghosh S., (2006), Multiple cohesive crack growth in brittle materials by the extended Voronoi cell finite element model, International Journal of Fracture, 141, pp. 373-393.
53. Chui C. K., Wang G. Z., (1991), A cardinal spline approach to wavelet, Proceeding of the American Mathematical Society, 113, pp. 785-793.
54. Hollister S. J., Kikuchi N., (1994), Homogenization theory and digital imaging: A basis for studying the mechanics and design, Biotechnology and Bioengineering, 43, pp. 586-596.
55. Tanaka S., Okada H., Okazawa S., (2012, A wavelet Galerkin method employing B-spline bases for solid mechanics problems without the use of a fictitious domain, Computational Mechanics, 50, pp. 35-48.
56. Chessa J., Wang H., Belytschko T., (2003), On the construction of blending elements for local partition of unity enriched finite elements, International Journal for Numerical Methods in Engineering, 57, pp. 1015-1038.
57. Shibanuma K., Utsunomiya T., (2011), Evaluation on reproduction of $priori$ knowledge in XFEM, Finite Elements in Analysis and Design, 47, 424-433.
58. Shibanuma K., Utsunomiya T. Aihara Shuji, (2011), Correction of incompleteness of XFEM Approximation (2nd report: Application to fracture mechanics), Transactions of JSCES, Paper No. 20110007. (in Japanese)
59. Liu Z. L., Menouillard T., Belytschko T., (2011), An XFEM/Spectral element method for dynamic crack propagation, International Journal of Fracture, 169, pp. 183-198.
60. Yau J. F., Wang S. S., (1984), An analysis of interface cracks between dissimilar isotropic materials using conservation integrals in elasticity, Engineering Fracture Mechanics, 20, pp. 423-432.
61. Rice J. R., (1968), A path independent integral and the approximate analysis of strain concentration by notches and cracks, Journal of Applied Mechanics, 35, pp. 379-386.
62. Stern M., Becker B., Dunham R. S., (1976), A contour integral computation of mixed-mode stress intensity factors, International Journal of Fracture, 12, pp. 359-368.
63. Murakami Y. ed., (1987), Stress intensity factors handbook, Pergamon Press.
64. Woo C. W., Wang Y. H., Cheung Y. K., (1989), The mixed mode problems for the cracks emanating from a circular hole in a finite plate, Engineering Fracture Mechanics, pp. 279-288.
65. Erdogan F., Sih G., (1963), On the crack extension in plates under plane loading and transverse shear, Transactions of the ASME, Journal of Basic Engineering, 85, pp. 519-527.
66. Norikura T., Murakami Y., (1983), Application of the body force method to the analysis of stress intensity factors and the prediction of crack propagation path under two-dimensional mixed boundary conditions, Transactions of the Japan Society of Mechanical Engineers (JSME), Series A, 49, pp. 818-828. (in Japanese)
67. Higuchi M., Kawahara M., Kondo K., Kurihara M., (1976), Simulation of two dimensional crack growth, Journal of the Society of Naval Architects of Japan, 139, pp. 221-226. (in Japanese)
68. http://www.pardiso-project.org/

DOI: 10.1002/nme